Journal Pre-proofs

Nitrogen oxide remediation through metal–organic frameworks with bi-functional absorption and photocatalytic characteristics

J. Teixeira, P.M. Martins, R. Fernández de Luis, E. Falletta, M.F. Ordoñez, C.L. Bianchi, S. Lanceros-Méndez

PII: S1385-8947(24)01887-4
DOI: https://doi.org/10.1016/j.cej.2024.150400
Reference: CEJ 150400

To appear in: *Chemical Engineering Journal*

Received Date: 5 November 2023
Revised Date: 3 March 2024
Accepted Date: 12 March 2024

Please cite this article as: J. Teixeira, P.M. Martins, R.F. de Luis, E. Falletta, M.F. Ordoñez, C.L. Bianchi, S. Lanceros-Méndez, Nitrogen oxide remediation through metal–organic frameworks with bi-functional absorption and photocatalytic characteristics, *Chemical Engineering Journal* (2024), doi: https://doi.org/10.1016/j.cej.2024.150400

This is a PDF file of an article that has undergone enhancements after acceptance, such as the addition of a cover page and metadata, and formatting for readability, but it is not yet the definitive version of record. This version will undergo additional copyediting, typesetting and review before it is published in its final form, but we are providing this version to give early visibility of the article. Please note that, during the production process, errors may be discovered which could affect the content, and all legal disclaimers that apply to the journal pertain.

© 2024 Published by Elsevier B.V.

Nitrogen oxide remediation through metal-organic frameworks with bi-functional absorption and photocatalytic characteristics

J. Teixeira[1,2,3], P.M. Martins[3,4], R. Fernández de Luis[7], E.Falletta[5,6], M.F.Ordoñez[5,6], C.L.Bianchi[5,6], S. Lanceros-Méndez[1,7,8*]*

[1] Physics Centre of Minho and Porto Universities (CF-UM-UP), and Laboratory of Physics for Materials and Emergent Technologies, LapMET University of Minho, 4710-057 Braga, Portugal,
[2] Centre/Department of Chemistry, University of Minho, 4710-057 Braga, Portugal
[3] Centre of Molecular and Environmental Biology, University of Minho, 4710-057, Braga, Portugal
[4] IB-S – Institute for Research and Innovation on Bio-Sustainability, University of Minho, 4710-057, Braga, Portugal
[5] Dipartimento di Chimica, Università Degli Studi di Milano, Via Golgi, 19, 20133, Milano, Italy
[6] Consorzio Interuniversitario Nazionale per la Scienza e Tecnologia dei Materiali (INSTM), Via Giusti 9, 50121, Florence, Italy
[7] BCMaterials, Parque Científico y Tecnológico de Bizkaia, 48160 Derio, Spain
[8] IKERBASQUE, Basque Foundation for Science, 48013 Bilbao, Spain

Abstract

In the population increase and growing industrialization framework, NO_x (NO and NO_2) arises among the most important air pollutants responsible for various health and environmental conditions. Metal-organic frameworks, MOFs, are promising materials for NOx remediation.

This study investigates the removal of nitrogen oxides (NOx) using metal-organic frameworks (MOFs). MOFs UiO-66, UiO-66-NH_2, MIL-125, and MIL-125-NH_2 were synthesized and characterized. The surface area of the MOFs was quantified, showing values like 1118 m²/g for UiO-66-NH_2 and 1424 m²/g for MIL-125-NH_2. The NOx removal efficiency using the NH_2 functionalized MOFs reached 100% efficiency under UV light. Moreover, the immobilization of MIL-125-NH2 in carrageenan/alginate matrices was investigated, maintaining significant NOx reduction capabilities ~ 80%. This work also emphasizes the potential of MOFs by combining adsorptive and photocatalytic properties, providing insights into NOx capture and transformation mechanisms, and proposing a viable approach for sustainable air remediation technologies. This work paves the way for the successful applications of MOFs and MOF-modified membranes for air pollution mitigation.

Keywords: *NOx; Metal-organic frameworks; porous membrane; adsorption; photocatalysis; natural polymers*

1. Introduction

Nowadays, society increasingly focuses on sustainable development, as defined by the United Nations in the seventeen "*Sustainable Development Goals*" [1]. Achieving zero-toxic air is a cornerstone challenge that directly or indirectly impacts the sustainability of our environment and society. Among the gas pollutants in the atmosphere above their natural background, nitrogen oxides or NO_x significantly affect humans' respiratory and immune systems, reaching alarming levels in large cities [2]. In addition, NO_x emissions are directly responsible for generating acid rain, smog, haze and ozone layer depletion [3-6].

Although NO_x is also naturally produced (e.g., volcanic activity, decomposition of organic matter, lightning, etc.), their emissions come predominantly from three anthropogenic activities: combustion of fossil fuels for transportation, combustion of natural gas, and manufacturing of nitrogen fertilizers [7-9]. NO_x remediation is challenging since the partial oxidation of NO and NO_2 can give rise to various inorganic and organic gaseous pollutants and radical species [10, 11]. Among the potential technologies under investigation, to eliminate NO_x from the atmosphere, selective catalytic [12-14] and non-catalytic reduction [15, 16], plasma-assisted reduction [17-19], and biological processes [20, 21] are the most commonly employed. Nevertheless, higher efficiencies are needed, characterized by high operation costs, complex maintenance, and limited capacity to process pollutants [22].

In this context, the adsorption approach offers advantages lacking in the abovementioned technologies. In particular, the microstructure and chemical properties of the sorbent materials can be tailored to promote specific physical-chemical interactions with the target gas molecules. Sorption-based technologies have already demonstrated their potential to capture or separate gases such as NO_x and SO_x in the air at ppb levels [23-26], further removing them from sorbent material via controlled thermal or vacuum desorption processes. [27]. This leads to adsorption being regularly considered an environmental-friendly, efficient, and economic strategy for NO_x removal in the presence of materials such as activated carbons [28-30], core-shell structures [31], metal oxides [32-35], and zeolites [36-39].

Despite its high efficacy, sorption consists of a mass transfer process by which a substance is transferred from a proper phase (liquid, gas or solid) to the surface of the solid sorbents. Therefore, when the sorbent reaches its saturation level, it must be regenerated. Further, the pollutant should be transferred to other treatments for the subsequent degradation or recovery, with a consequent increase in process costs [40].

Advanced oxidation processes (AOP), such as photocatalysis, offer exciting possibilities. The light-induced oxidation of NOx is triggered by the generation of strong oxidizing and reducing species on a photocatalyst's surface due to the photon adsorption and posterior charge carrier's migration within its structure [41, 42]. The main advantage of this approach is the possibility of oxidizing NOx into NO_3, which is easily removable from the surface of the photocatalyst by washing it with water. For instance, traditional photocatalysts, such as TiO_2 [43, 44] and ZnO nanoparticles (and other functionalized or hybrid nanomaterials) [45, 46], among others [47-52], have demonstrated their efficacy in facing a green and cost-effective NOx decontamination under visible and solar energy

illumination, always within certain operational conditions still far from the ones found in real scenarios. The central negative aspect of photocatalytic materials is their complete inactivity without light irradiation.

Overall, there is room for improvement in the selectivity, capacity and reusability of classic porous materials and photocatalysts to capture and transform NO_x from the air [53]. For this reason, coupling adsorption to photocatalytic oxidation NO_x in a dual approach could overcome the drawbacks of applying single technologies. Here is where Metal-Organic Frameworks (MOFs) can play a relevant role when compared to classic sorbents and photocatalysts due to their tuneable porosity (i.e., in terms of surface areas, pore size and chemistry) and tailorable semiconducting characteristics. MOFs are inorganic-organic materials built up from inorganic metal ions or clusters connected through organic linkers in an ordered and robust fashion [54-57]. Their inorganic and organic blocks can be modified to enhance their light-harvesting capacity, promote the charge carriers' migration through their structure, and tune their pore chemistry to specifically interact with the target molecule to be trapped or transformed. Given their unique versatility, numerous MOFs (ZIF-8 and Mg-MOF-74 [58], ZIF-67 [59], and different Fe-based MOFs [60], among others [61]) have been applied in air remediation of organic volatile compounds by combining adsorption and photocatalytic degradation. These exhibiting open metal sites, such as Fe^{III} [62], Cu^{II} [63] or Co^{II} [64] based MOFs, have shown exceptional performance for NO_x chemisorption since nitrogen oxides coordinate these positions during their capture.

Nevertheless, they have shown poor chemical stability in the long term or upon cycling. In contrast, MOFs based on tetravalent ions, such as Zr(IV)-UiO-66 (UiO: University of Oslo) and Ti(IV)-MIL-125 (MIL: Materials Institute Lavoisier), have shown promising results as sorbents and photocatalysts towards NO_x as well as interesting hydrolytic stability needed for their application for air remediation [60, 61] [65, 66]. Despite these relevant characteristics and their chemical versatility due to their defect chemistry and pre- or post-synthetic encoding possibilities, UiO-66 and MIL-125 have been scarcely explored for the combined adsorption and photooxidation of NO_x to NO_3^-. In this research, we have synthesized UiO-66, UiO-66-NH_2, MIL-125 and MIL-125-NH_2 compounds under reflux conditions to test their efficiency for NOx removal later. In addition, to give further steps in the system's applicability, we have immobilized the best of the studied materials into a biopolymeric matrix shaped as an air filtering system and compared its performance with the parent powdered material.

2. Experimental

2.1. Chemicals

Zirconium(IV) chloride 99.5% was purchased from Alfa Aesar; Titanium(IV) isopropoxide ($Ti(iPrO)_4$ 97%), N,N-dimethylformamide (DMF 99.8%), terephthalic acid, and amino terephthalic acid (BDC 97% and BDC-NH_2 99% respectively) were purchased from Sigma Aldrich. The chemicals were used without modifications. Sodium Alginate and ι-Carrageenan were bought from Merck. Deionized water was processed in a Milli Q Integral 5 system.

2.2. Synthesis and Characterization of the Metal-Organic Frameworks

- UiO-66 and UiO-66-NH_2

UiO-66 was produced via a reflux solvothermal process. First, zirconium chloride (0.5418 g, 3.334 mmol) was dissolved in DMF (30 mL) under stirring. After this, a solution of terephthalic acid (0.38012 g, 2.289 mmol) in DMF (30 mL) and distilled water (1.5 mL) were added dropwise to the zirconium chloride solution while stirring. The reaction media was left under stirring at 80 ºC. After 24 hours, the material was recovered via centrifugation (at 6500 rpm for 10 minutes), thoroughly washed with DMF (100 mL, three times each) and methanol (100 mL, three times each), and left to dry at 80 ºC for another 24h. UiO-66-NH_2 was obtained following the same protocol but using 0.42 g (2.318 mmol) of BDC-NH_2 instead of BDC.

- *MIL-125 and MIL-125-NH_2*

MIL-125 was synthesized via the reflux protocol described by Sohail et al. [67]. In this procedure, terephthalic acid (7.70 g, 46.4 mmol) was dissolved in DMF (100 mL) under reflux conditions (100 °C) for one hour under stirring. Afterwards, 28 mL of methanol was added to the solution, stirring for another hour. Finally, titanium isopropoxide (8.4 mL) was added dropwise, yielding a white precipitate immediately after the mixture. The reaction was refluxed for three days, recovered, and washed with DMF and ethanol (250 mL, three times each). After washing, the processed material was dried at 80 °C for 24 hours. MIL-125-NH_2 was obtained following the same protocol but using 8.40 g (46.37 mmol) of BDC-NH_2 instead of BDC.

2.2.1. MOF characterization

The morphology of the MOF nanoparticles was observed by Scanning Electron Microscopy (SEM) (JEOL JSM-7000F) operating at 10 kV. Before analysis, the samples were coated with a gold layer of 15 nm using the Quorum Q150TS turbo-pumped coater.

The crystal structure of the MOFs was evaluated by X-ray diffraction. The powder X-ray diffraction (PXRD) patterns of the MOF samples were measured at room temperature using a Panalytical X´pert CuKα diffractometer in the following conditions: 2θ range = 5–70°, step size = 0.05°, exposure time = 10 s per step. Full peak fit profile matching of the MOF samples was performed. The final fittings are shown in Figure S1, supplementary information.

Fourier-transform infrared spectroscopy (FTIR) spectra were measured using a Jasco FT/IR-6100 spectrometer in Attenuated Total Reflectance mode (FTIR-ATR). Each spectrum was recorded from 600 to 4000 cm^{-1} with a 1 cm^{-1} resolution. 64 scans were measured and averaged to obtain the final spectra.

Thermogravimetric analysis (TGA) was performed under synthetic air (25 mL/min) with a Netzsch STA 449F3 DSC–TGA thermo-balance instrument. This equipment allows the

adjustment of the heating rate, control of the measured atmosphere, and selection of the temperature program. An alumina crucible containing ca. 25 mg of the sample was heated at 5 °C min^{-1} in the 30–700 °C temperature range.

Thermogravimetric analysis was also employed to quantify the defect degree within the UiO-66 MOF structure. The average linker-defect positions per formula were estimated from the weight loss associated with the organic linker calcination step (at an approximate temperature of 300ºC). Suppose the complete dehydration of the zirconium hexanuclear clusters occurs before the organic linker calcination step. In that case, the theoretical weight loss associated with the linker release as a function of the defect degree can be calculated based on the following equation:

$$Zr_6O_{6+x}(Linker)_{6-x} \rightarrow Zr_6O_{12} \qquad \text{(Equation 1)}$$

where X is the defect degree [68]. The theoretically calculated data can be fitted to a linear equation (Figure S2b) that has been used to determine the experimental defects per formula from the experimental weight loss obtained from the thermogravimetric curves.

UV-Vis spectra were obtained with a Shimadzu UV1800 in the range of 200-2200 nm to assess the light adsorption range of the MOFs.

CO_2 sorption isotherms were measured at 273 K using a Quantachrome ISorb instrument. Approximately 10-20 mg of the MOF particles were degassed at 200°C under a high vacuum (<0.0005 bar) for at least 12 h before the measurement. The surface area value was obtained by fitting the adsorption data to a linearized form of the Brunauer–Emmett–Teller (BET) equation [69]. The correlation coefficients were higher than 0.999 for all samples. Results are shown in Figure S3.

2.3. Immobilization of the MOFs into alginate/carrageenan porous membranes

2.3.1. Membrane preparation

Sodium alginate and ι-carrageenan, in a ratio of 1/1, performing a total polymer weight ratio of 2% in water, were stirred in deionized water until complete dissolution, following the procedure of Li et al. [70]. The concentration chosen was based on previous works to obtain a better trade-off between porosity and mechanical properties. The solution was left to rest for three hours to remove air bubbles. Afterwards, the solutions were frozen at -80 °C in a Panasonic Ultra-Low Temperature Freezer for 24h, then dried in a Labconco FreeZone 2.5 freeze drying machine for another 48h. The same protocol was followed to obtain composite MOF- Alginate/carrageenan air filters by dispersing the MOF particles into the alginate/ι-carrageenan water solution. To this end, the dispersion was sonicated for one hour before freezing at -80 °C. A membrane with a final thickness of 2.36±0.1 mm was obtained.

2.3.2. Membrane characterization

The morphology of the MOF nanoparticles was observed by Scanning Electron Microscopy (SEM) (JEOL JSM-7000F) operating at 10 kV. The samples were coated with a gold layer of 15 nm using the Quorum Q150TS turbo-pumped coater.

Fourier-transform infrared spectroscopy (FTIR) spectra were measured using a Jasco FT/IR-6100 spectrometer in Attenuated Total Reflectance mode (FTIR-ATR). Each spectrum was recorded from 500 to 4000 cm^{-1} with a 1 cm^{-1} resolution. 64 scans were measured and averaged to obtain the final spectra. The thermal properties of the samples were determined by differential scanning calorimetry (DSC) using a Mettler-Toledo DSC 822e. Stress-strain measurements were performed in a TST350 Linkam Instruments device at a strain rate of 15 ms^{-1} to assess the mechanical characteristics at room temperature.

2.4. NO_x removal assays

The NO_x removal tests took place inside a 25 L homemade reactor (described schematically in Figure 1) under dark and irradiation (500 W halide lamp emitting in the UV-A (320–400 nm) conditions with an intensity of 20 W/m². The NOx concentration was monitored over time (0 to 180 minutes for each test), tested with different initial pollutant concentrations (500, 750 and 1000 ppb; ± 50 ppb) and sorbent/catalyst ratios (10, 25 and 50 mg). The NOx concentration was determined with a chemiluminescence analyzer (ENVEA AC32e). Photolysis test results were negligible (< 5% of pollutant degradation after 3 h of light irradiation).

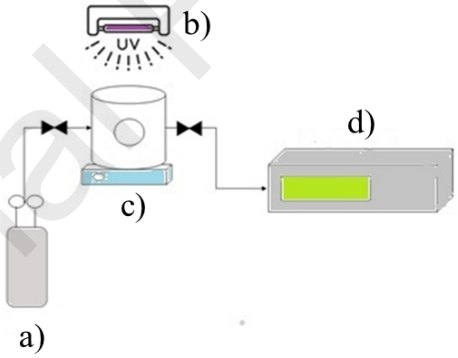

Figure 1 – Schematic representation of the NOx removal reactor setup. a) NO_x tank; b) UV-lamp; c) homemade reactor; d) NOx analyser.

Journal Pre-proofs

3. Results and Discussion

3.1. Active materials characterization

The morphological, structural, physical-chemical and optical properties of all the synthesized materials were evaluated using scanning electron microscopy (SEM), X-ray diffraction (XRD), Infrared spectroscopy (IR), thermogravimetric analyses (TGA), UV-Vis spectroscopy (UV-Vis) and 273K-CO_2 adsorption isotherms. The results have been summarized in Figures 2, 3 and S3-4.

First, the morphology of the synthesized MOF materials was investigated via scanning electron microscopy (Figure 2). SEM images show that UiO-66 and MIL-125 exhibit different particle sizes and morphologies. UiO-66 and UiO-66-NH_2 crystallize as agglomerated spherical particles of almost identical sizes (55±14 nm for UiO-66 and 59±18 nm for UiO-66-NH_2, respectively).

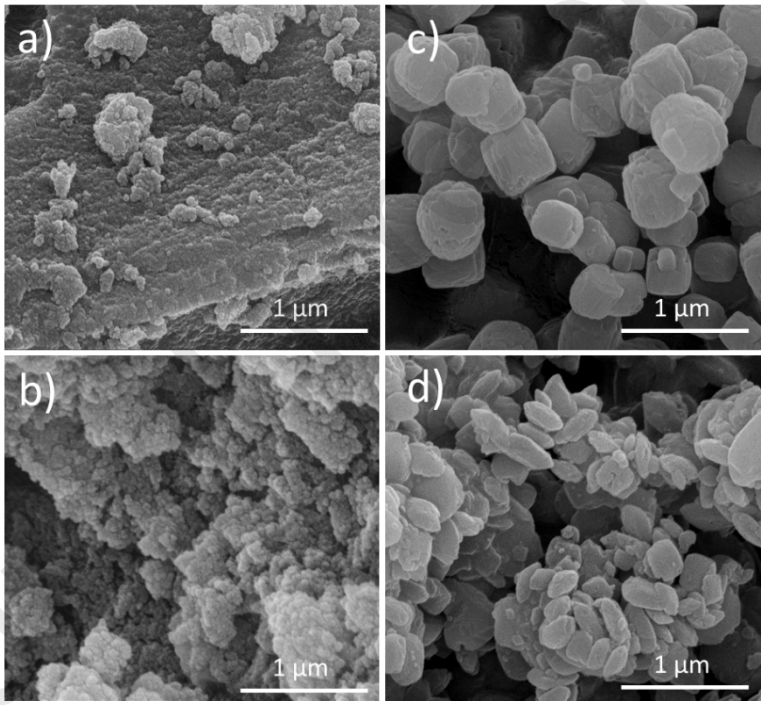

Figure 2 – SEM images of a) UiO-66, b) UiO66-NH_2, c) MIL-125, d) MIL-125-NH_2.

In contrast, MIL-125 exhibits particles with cube-like morphologies with diameters ranging from 245 to 620 nm. By statistically analyzing the sample, an average diameter of 453±96 nm is obtained for the MIL-125 sample. On the other hand, even if the synthesis conditions are similar to the ones of MIL_125, MIL-125-NH_2 crystallizes as a mixture of cube-like and elongated octahedral particles. The particle diameter is lower than the one observed for MIL-125, with values ranging from 130 to 430 nm and an average of 279±67 nm [67].

Regarding the long-range order of the samples, the experimental X-ray diffraction data (Fig. 3a) are consistent with the patterns simulated from the structural models reported in the Cambridge Structural Database for UiO-66, UiO-66-NH_2, MIL-125, and MIL-125-NH_2 [68]. The XRD signature of UiO-66 and UiO-66-NH_2 is related to the archetypal cubic structure of these zirconium-based MOFs. In brief, the hexanuclear $[Zr_6O_4(OH)_4]$ oxo clusters are connected through twelve organic linkers, giving rise to a cubic framework with an Fm-3m symmetry, a cell parameter close to 20.7 Å, and a fcu topology [67, 70, 71]. The simulated and experimental XRD patterns show the most intense diffraction maxima at approximately 8° (111), 9° (200), and 25° (422) in 2θ (°). The two strong diffraction maxima at low 2θ (7.4 ° and 8.6 °, respectively) confirm that UiO-66 has been obtained just in the cubic phase, excluding other possible polymorphic forms within the sample [71]. Further, the absence of additional diffraction maxima apart from the ones of UiO-66 further discards impurities in the samples. Also,

Similarly, the experimental XRD patterns of MIL-125 and MIL-125-NH_2 show the characteristic maxima ascribed to the orthorhombic crystal structure of the MIL-125 materials (2θ = 7° (110 and 101), 10° (200) and 12° (211)) accordingly to results previously reported [72]. A full profile fitting of the patterns was carried out to analyze the XRD data further, starting from the cell parameters and the space groups typically reported for UiO-66 and MIL-125. As expected, the profile matching analysis fits the experimental data well, with only a significant variation of the maxima's width related to reduced crystalline domains usually ascribed to smaller particle sizes.

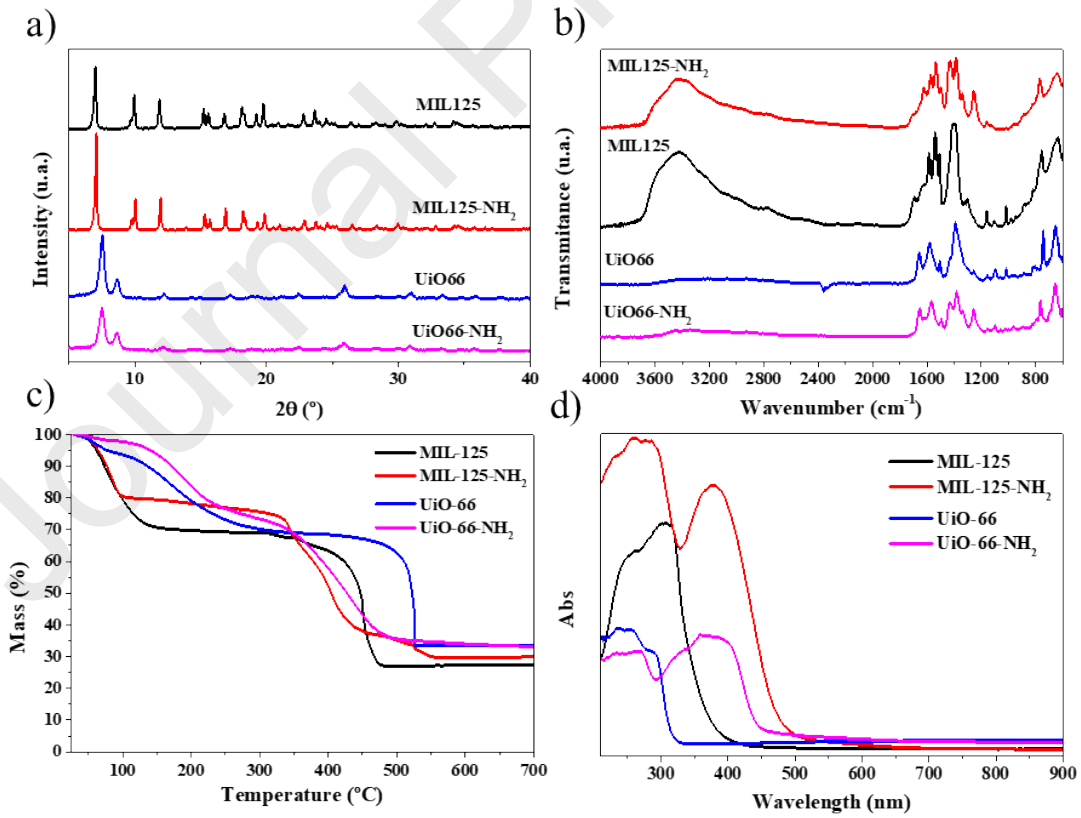

Figure 3 – XRD patterns (a), FTIR spectra (b), TGA (c), and UV-spectra (d) of MIL-125, MIL125-NH_2, UiO66, and UiO66-NH_2.

CO_2 adsorption isotherms at 0 ºC from 0 to 30 bars were performed to estimate the surface area of the compounds. As shown in Figure S3, the CO_2 isotherms exhibit the The type-I profile was ascribed to microporous materials in the low-pressure regimes (P= 0 – 5 bars) and a second increase in uptake at higher pressures related to the interparticle capillary condensation of the CO_2. The Brunauer–Emmett–Teller (BET) surface area was calculated by fitting the data between 0.1 to 0.2-0.3 bars with the linearized form of the BET equation [69]. The surface areas agree with previous reports, with values for UiO-66, UiO-66-NH_2, MIL-125 and MIL-125-NH_2 of 1241, 1118, 1485 and 1424 m^2g^{-1}, respectively [68]·[73]. The values for the surface areas are within the usual ranges reported in the bibliography but still lower than the calculated theoretical values obtained from the crystallographic models. Still, the IR spectra of the thermally treated (200ºC) samples show a small contribution of the possible solvent or uncoordinated organic linkers trapped within the pore space of our materials. Thus, most of the porosity is accessible for NOx species, as it will be explained later in detail during the adsorption and photo-oxidation experiments.

Concerning the FTIR data (Fig. 3b), the spectra for UiO-66 and UiO-66-NH_2 possess intense bands at around 1580 and 1390 cm^{-1}, congruent with the symmetric and asymmetric stretching vibrations of the carboxyl groups of the terephthalic ligand. In contrast, the weak signal at around 1500 cm^{-1} corresponds to the C=C vibrations of the benzene ring [74]. At lower frequencies, the stretching vibration of the bonds Zr-$O_{\mu 3\text{-}O}$ (655 cm^{-1}) of the [$Zr_6(O)_4(OH)_4$] clusters is observed [75]. The main difference between UiO-66 and UiO-66-NH_2 is a prominent band at 1253 cm^{-1}, characteristic of the C-N stretching vibrations related to the amino groups [76]. The FTIR spectra of MIL-125 and MIL-125-NH_2 present the well-defined bands associated with the asymmetrical and symmetrical vibrations of carboxylate groups from 1700 to 1500 cm^{-1} and 1400 to 1300 cm^{-1}, respectively. Moreover, additional bands appear at low-frequency (800-600 cm^{-1}) attributed to O-Ti-O vibrations [77]. It is worth noting that the wideband between 3600 and 2500 cm^{-1} is due to the solvent entrapped within the pores of the as-synthesized materials [78]. The thermal treatment of the samples up to 200 ºC reduces the broadband associated with water moisture and organic solvents trapped within the porosity. At 200ºC, the signatures related to the IR region's C-H, -OH and NH_2 vibrational modes are revealed. Still, slight variations in the intensity and position within the bands located at the low-frequency regions are also observed. As concluded from temperature-dependent IR data, the dehydration/de-solvation of the materials mainly occurs between room temperature and 100-150ºC, with the IR bands associated with the vibrational band of the framework components unaffected. Above 150ºC, significant variations in the relative intensity and positions of several absorption maxima, specifically those related to the Zr-O and Ti-O structs, are observed. This finding points to the dehydration/de-solvation process of water, solvent or modulator species coordinatively bonded to the metal ions of the framework (Figure S4).

The thermal behaviour of the four MOFs was studied by thermogravimetric measurements (Fig. 3c). Both UiO-66 and UiO-66-NH_2 present a three-step loss, and the first process occurs between room temperature and 100 °C, associated with the release of the water molecules. The second step, which extends from 130 °C to 350 °C, corresponds to the elimination of solvent molecules trapped within the pore space of the material

together with the dehydration of the $Zr_6O_4(OH)_4$ clusters. At 350 ºC, the dehydration of the inorganic clusters is concluded. Thus, the chemical formula of the UiO-66 and UiO-66-NH_2 materials can be expressed as $Zr_6O_{6+x}(linker)_{6-x}$, where x is the average number of linker defects present on the crystal structure [79, 80]. These linkers' defects can be estimated after equation 1, given the last step of the thermal degradation of the UiO-66 and UiO-66-NH_2 compounds (Figure S2), corresponding to the organic linkers' calcination [68]. Considering the calculated and experimental weight losses observed from 350 ºC to 500 ºC, 0.5 and 0.9 linkers' defects per formula unit have been estimated for the UiO-66 and UiO-66-NH_2 materials. The last step is the decomposition of the frameworks, leading to the crystallization of ZrO_2. UiO-66 appears more thermally stable than its NH_2 form, losing most of its mass at 500 °C.

MIL-125 and MIL-125-NH_2 present a TGA curve with two-step weight losses [81, 82]. The first one, from 80 to ≈150 °C, corresponds to the loss of water and the release of other solvent molecules related to the synthesis process that remain in the pore space of MIL-125 and MIL-125-NH_2 materials. This dehydration step results in a solvent-free structure that is stable up to 350 °C, the temperature at which the decomposition of the organic linkers (either terephthalic or amino terephthalic acid) begins.

Finally, UV-Vis spectroscopy was performed to evaluate the materials' optical properties (Fig. 3d). The UV-vis spectrum of UiO-66 reaches its maximum adsorption at 243 nm, attributed to the ultraviolet absorption from the ligand to metal charge transfers within the zirconium oxoclusters [83]. It is worth noting that the presence of the NH_2 groups in UiO-66-NH_2 and MIL-125-NH_2 endows them with a second UV-Vis absorption feature approximately located at 375 nm. This comes from the light adsorption of amino-terephthalic linkers within their frameworks [68]. For instance, amino groups act as light-harvesting antennas that transfer the holes and electrons to the inorganic clusters of the UiO-66 and MIL-125 frameworks. In contrast, the spectrum of MIL-125 shows a strong absorption band at 305 nm (UV region), induced by the ligand-to-metal charge transfer of O to Ti in the inorganic clusters of $TiO_5(OH)$ [84].

3.2. NOx removal assays

To assess the multifunctionality of the UiO-66 and MIL-125-based MOFs to adsorb and photo-oxidize NOx concurrently, the samples were introduced in a 25 L reactor (Figure 1), exposed to NO_x and tested both under dark and illumination conditions. Two parameters were evaluated during the experiments: the initial concentration of NO_2 and NO_x (from 500 to 1000 ppb) and the MOF adsorbent/photocatalyst dosage (10/25/50 mg) (Figures S5-S9 in the supplementary information). The results in Figure 4 show the efficiency in removing 1000 ppb of NO_2 and NO_x when using 50 mg of MOF material under dark and illumination conditions. The results from the additional experiments performed with lower MOF loadings and lower NO_x and NO_2 concentrations are presented as supplementary material in figures S5 to S9.

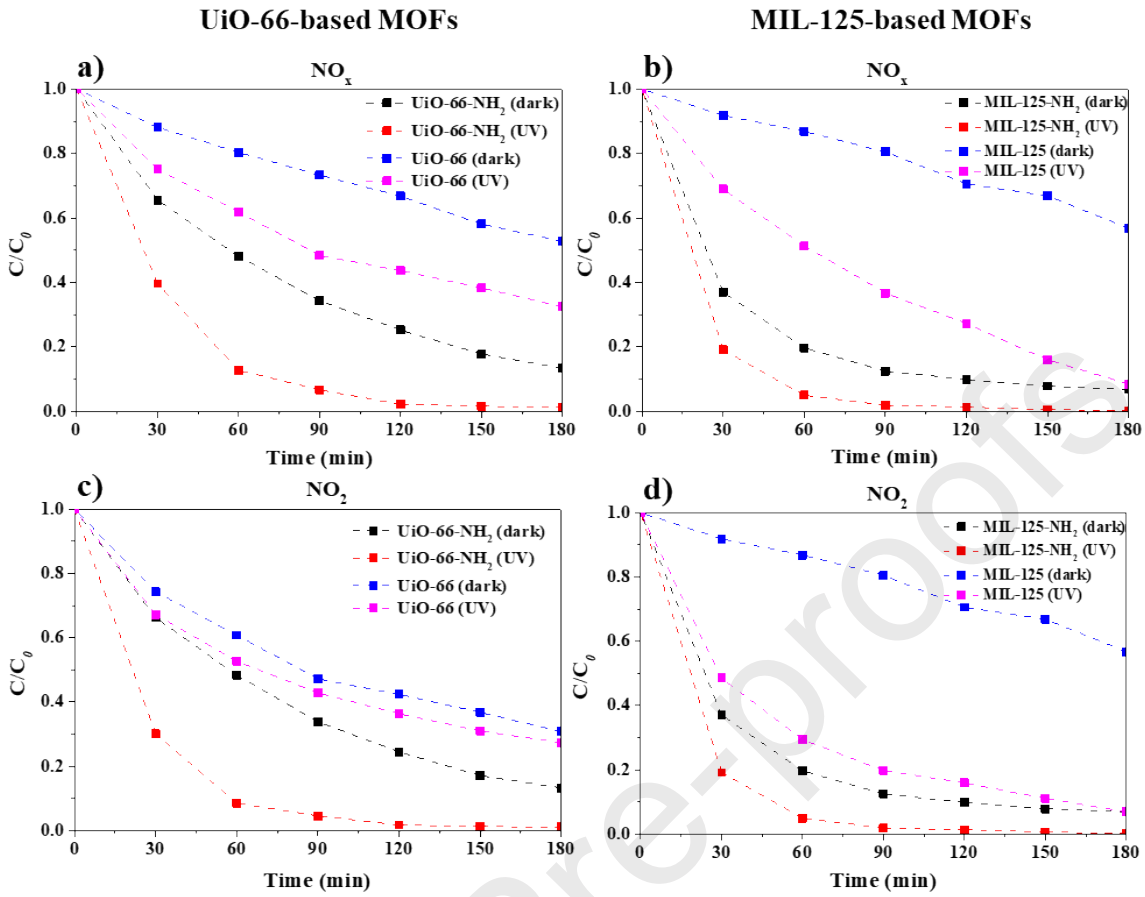

Figure 4 – Normalized graphics of adsorption/photodegradation of NO_2 and NOx efficiencies for the synthesized MOFs. a) and c) represent the results for the UiO-66-based MOFs. (b) and (d) show the results for the MIL-125-based MOFs—initial concentration of NOx 1000±50 ppb.

3.2.1. Adsorption in dark conditions

As reported before, the adsorption properties of the synthesised MOFs towards NO_x were investigated in dark conditions. As shown in Fig. 4a-b, UiO-66 and MIL-125 do not exhibit high activity, leading to a NO_x reduction below 40% in 180 minutes. In contrast, the presence of the NH_2 groups on their frameworks has a beneficial effect on the adsorption properties of the materials, doubling the percentage of both NO_2 and NO_x removal, which was *ca*. 80% for both MIL-125-NH_2 and UiO-66-NH_2 (Fig. 4a-b). The enhanced performances observed for the NH_2-modified MOFs can be ascribed to interactions between MOFs and pollutants, including van der Waals' forces, hydrogen bond formation, π-donation coordination, and acid-base interactions [53, 85]. In general, two main adsorption mechanisms prevail for NO_x removal by MOF structures: Bronsted-Lowry acid-base and Lewis acid-base chemical interactions, where the former is observed when amine groups are grafted on the MOFs' structures [86-90], whereas the latter is related to the presence of open metal sites [91, 92]. In the present case, it is evidenced that the amino groups act as typical chemical bases for acid-gas adsorption. For this reason, their presence in the MOF structure is essential to obtain improved NO_x removal activity, as illustrated in Figure 5(A-B).

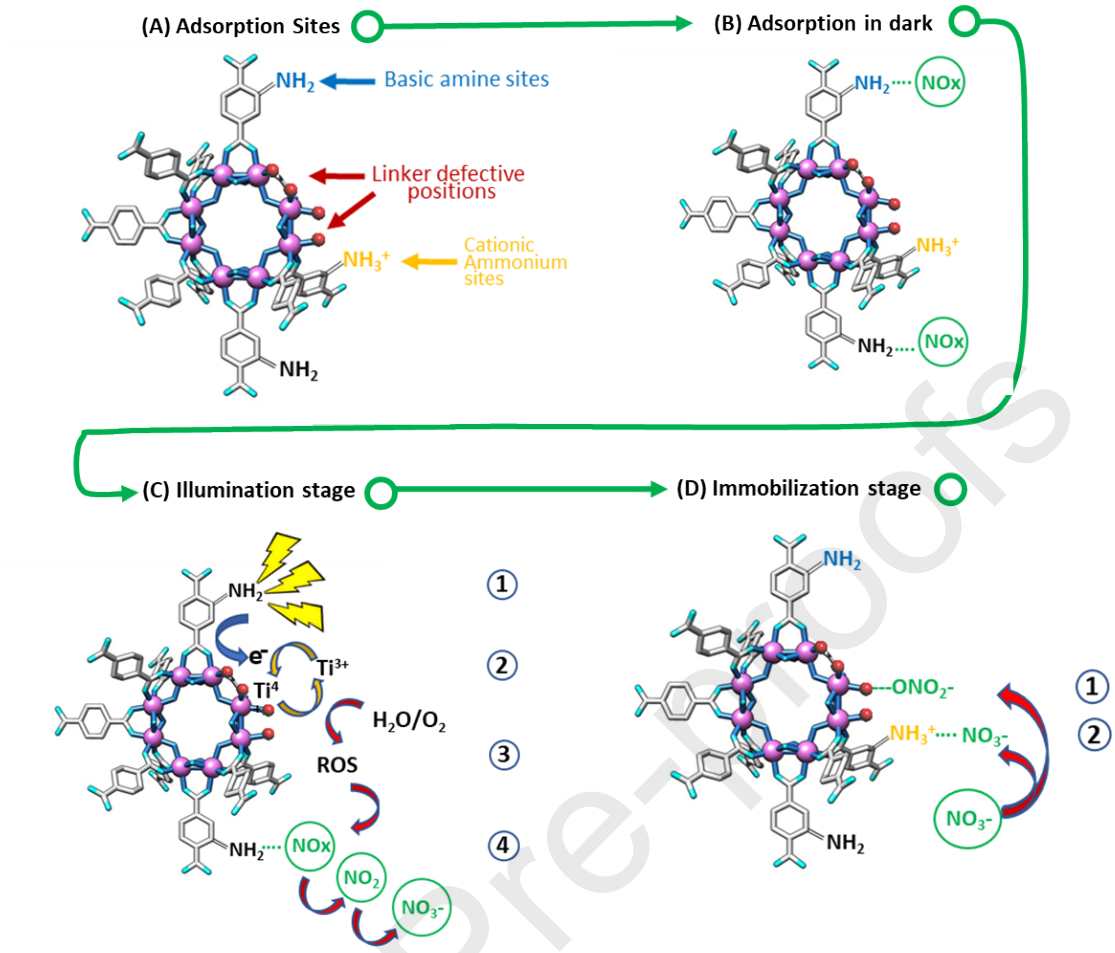

Figure 5 – Schematic representation of the (A) Adsorption sites and (B) NOx adsorption, (C) photo-oxidation and (D) immobilization mechanisms in MIL-125-NH_2.

Our work aligns with previous results reported in the literature for NO_2 and NO_x adsorption with MOFs, summarized in Table 2. UiO-66 and UiO-66-NH_2 have already been tested for NO_2 adsorption in continuous flux conditions, showing adsorption capacities of 20.3 and 31.2 mmol g^{-1}, respectively [93-95]. In parallel, the importance of the defective positions and their post-synthetic encoding has already been proven in UiO-66 and UiO-66-ox materials applied for NO_2 and NO_x capture. In brief, defect engineering has less impact on their adsorption capacity than the framework decoration with basic amine motifs. As previously demonstrated, NO_2 capture involves multi-step reactions with NH_2, forming diazonium ions and nitrosation-like chemisorption [86]. In addition, relative humidity is a pivotal parameter in enhancing NO_2 uptake by MOFs, as demonstrated for UiO-67 materials [88].

As concluded from the state of the art summarized in Table 3, there is still room for investigation to elucidate the structural robustness of Zr-MOFs in the presence of NO_x and NO_2, mainly if they are to be applied under humid conditions [86]. As an illustrative example, MOFs based on divalent ions such as copper-HKUST-1 [96, 97] perform outstandingly for the adsorption of NOx, but their chemical stability in humid conditions is in question. Highly robust MOFs based on more acidic metal centres have also been tested for NO_2 and NO_x capture, as in Al-MFM-300 [98] or metalloporphyrin-MOFs [99]. In contrast with previous experiments, our work has evaluated the dual photo-oxidation

and adsorption capacity of Zr and Ti-benchmark MOF materials in static conditions and under UV irradiation, being adsorption and photocatalysis stages studied individually to propose a NOx transformation and stabilization mechanisms of NOx within the MOFs.

Table 1 – MOFs investigated for NO_2 adsorption, dependence on initial NO_2 concentration and contact time.

MOF	Initial NO_2 Concentration	Adsorption efficiency (mmol g^{-1})	Contact Time (min)	Ref
U-ZrBDC	500-1000 ppm	2.2	300	[86-90, 100]
M-ZrBDC	"	0.22	"	"
U-ZrBDPC	"	3.35	"	"
M-Zr-BDPC	"	2.02	"	"
UiO-66-vac	2138 ppm	3.9	2000	[101, 102]
BPL/C	500-700 ppm	15.6	-	[86]
Ce-UiO-66	20-200 ppm	2.07	250	[103]
Ce-UiO-67	"	1.87	"	"
Urea modified UiO-66	20-200 ppm	0.8; 1.61	250-400	[86, 87, 89, 90, 104]
Melamine modified UiO-66	"	0.06; 0.89	"	"
V-MFM-300	350 ppm	13.0	250	[105]
Al-MFM-300	"	14	"	"

Journal Pre-proofs

MIL-125	Present work	2.1	180	Present work
MIL-125(NH_2)	Present work	4.2	"	Present work
UiO-66	Present work	2.0	"	Present work
UiO-66-(NH_2)	Present work	4.9	"	Present work

3.2.2. Photo-oxidation-driven transformation and capture of NOx

UV-light promotes a faster and more efficient conversion and capture of NO_x, especially for UiO-66-NH_2 and MIL-125-NH_2 variants, which show a 100% efficiency for NO_2 and NO_x removal after 90 minutes of irradiation, as represented in Figure 4. As shown in UV-Vis adsorption spectra (Figure 2b), NH_2 promotes the appearance of a sharp adsorption band around 375 nm for UiO-66-NH_2 and MIL-125-NH_2, a feature that makes them more efficient for the absorption of the light applied in the reactor-system (UV-A - 320–400 nm), and hence for the generation of reactive oxygen species that trigger the transformation of NO_x. Also, a competitive process between adsorption and photodegradation of NO_x occurs in the first 30 minutes under UV-light irradiation (Fig. 4 a) and b)), leading to adsorption and probably oxidation of NO_x and NO_2 to NO_3^-. The Kinetics of the photocatalysis and adsorption processes were analyzed in detail in the next step. Over the years, it has been reported that the Langmuir-Hinshelhood (L-H) model adequately describes the photocatalytic breakdown rate of different organic molecules [106-110]. The commonly used L-H model for photocatalytic degradation rate is represented by Equation 2:

$$r_{MOF} = -\frac{dC_{MOF}}{dt} = \frac{k_r K \cdot C}{1+K \cdot C} \quad \text{(Equation 2)}$$

Where r_{MOF} is the reaction rate, C_{MOF} is the concentration of the MOF, k_r is the reaction rate constant, and K is the Langmuir adsorption constant. Further, pollutant's concentration significantly impacts environmental remediation processes [111]. As a result, it is essential to assess how initial pollutant concentration affects the Kinetics of degradation [112]. Integration of Equation (2) results in a pseudo-first-order kinetics process at low gas concentrations (Equation 3) [107, 108]:

$$ln\frac{C_0}{C} = k_r K \cdot t = k_a \cdot t \quad \text{(Equation 3)}$$

Rearranging the terms of the equation, k_rK can be written as k_a, which is the pseudo-first-order reaction rate constant. Thus, a straight line resulting from the linearized plotting of ln (C_0/C) vs time allows the ka value to be obtained from the slope [112-114].

Figure 6 shows the final fittings of the linearized data for photocatalytic degradation kinetics studies of NOx (1000 ppb) by the MOF (50 mg) materials explored in this investigation. The effects of (I) the catalyst loading with a fixed concentration of NOx (i.e. 1000 ppb) (Figures S10 and S11) and (II) the initial concentration of NOx (500 and 750 ppb) for a fixed catalyst loading (Figure S12-S13) have been determined.

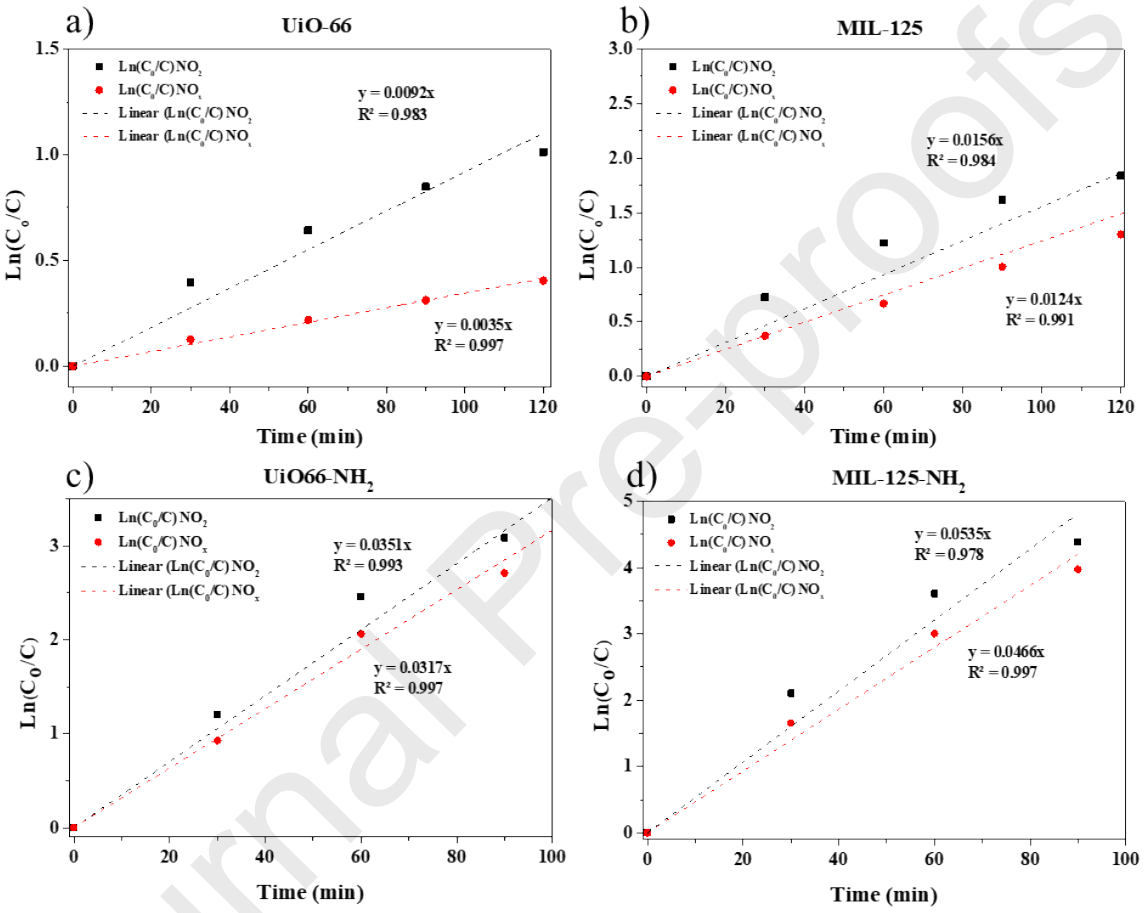

Figure 6 – Photocatalytic kinetic studies for the different synthesized MOFs. On the left, a) and c) are the results for UiO-66-based MOFs. On the right, (c) and (d) are the results for the MIL-125-based MOFs—catalyst mass: 50mg and initial concentration of NOx 1000±50 ppb.

As seen from the fittings of Figure 6, R^2 is over 0.98 in all cases, demonstrating the L-H approach's suitability for the system's description. A sharp increase in the k_a values is observed when both MOFs are functionalized with the $–NH_2$ group. In the case of UiO-66, adding the amine group increases these values by one order of magnitude, from 0.0092 for NO_2 and 0.0035 for NO_x, to 0.0351 and 0.0317 for NO_2 and 0.0317 for NO_x, respectively. The same happens for MIL-125, with values increasing almost five-fold for NO_2 and NO_x when NH_2 is added to the MOF. Table 2 summarizes the k_a values obtained for different catalyst loadings (10, 25 and 50 mg), using the concentration mentioned

Journal Pre-proofs

earlier of 1000 ppb and the respective R^2 for NO_x and NO_2 conversion. Information about k_a values for 500 and 750 ppb is presented in the supplementary information in Table S1.

Table 2 – Photocatalysis kinetics data obtained for NO_x and NO_2 conversion for the different synthesized MOFs. Initial concentration of NO_x: 1000±50 ppb

Sample	Catalyst mass (mg)	k_a NO_2 (min^{-1})	R^2, NO_2	k_a NO_x (min^{-1})	R^2, NO_x
UiO-66	10	0.0090	0.9884	0.0029	0.9787
	25	0.0117	0.9795	0.0048	0.9843
	50	0.0092	0.9830	0.0035	0.9970
UiO-66-NH_2	10	0.0195	0.9965	0.0181	0.9948
	25	0.0391	0.9965	0.0354	0.9983
	50	0.0351	0.9934	0.0317	0.9978
MIL-125	10	0.0118	0.9812	0.0080	0.9976
	25	0.0280	0.9872	0.0242	0.9911
	50	0.0156	0.9865	0.0124	0.9900
MIL-125-NH_2	10	0.0231	0.9971	0.0218	0.9902
	25	0.0463	0.9710	0.0454	0.9733
	50	0.0535	0.9783	0.0466	0.9923

The k_a values show an increase with the addition of the -NH_2 group for UiO-66 and MIL-125. This group allows the MOF to interact with the pollutant more effectively by conferring more active sites. Further, the BET data indicate that the MIL-125-based MOFs possess a larger surface area than the UiO-66-based ones, contributing to more efficient adsorption kinetics. In addition, the titanium-oxo nodes in MIL-125 prove to have a more efficient activation under UV-Vis light than zirconium-oxo building units of

UiO-66 materials. An analysis of Tables 2 and S1 shows that the kinetic constant decreases for each material as NOx concentration and catalyst loading increase. This may be due to a heterogeneous catalyst distribution that produces agglomerates and prevents total UV light irradiation and the progressive saturation of the MOF's active sites.

To demonstrate the effective NO_x photo-oxidation capability of the synthesized materials, they were subjected to FTIR analyses after the photocatalytic tests. Figure S14 compares the FTIR spectra of UiO-66 fresh and after six reuses (NO_x photodegradation tests). This approach was necessary due to the overlap of many typical signals of the nitrate ion with those of the MOF. However, in the UiO-66 FTIR spectrum, the shoulder at 1385 cm^{-1} and that at 1431 cm^{-1}, which are ascribable to nitrate ions, is evident [115, 116].

From the results reported up to date for MOFs as dual sorbents and photocatalysts for NO_x and NO_2 remediation, the ones reported in this study stand out because of their efficiency even when the studied MOFs have not been subjected to any further metal-doping or hybridization, as summarized in Table 4 [117, 118]. It is worth noting that all the synthesized materials show very high activity toward NO_x capture and degradation. However, the experiments have been performed in highly dissimilar conditions regarding initial NOx concentration, catalyst loading, and illumination sources.

Table 3 – MOFs investigated for NOx photodegradation and percentage of NOx degraded.

MOF	Initial NOx Concentration (ppb)	Nox degradation (%)	Time (min)	Ref
Fe-MIL-101	350-400	61	150	[7]
(Fe-MIL-88B)	"	61	"	[7]
(Fe-MIL-53)	"	77	"	[7]
Ru-NH_2-UiO-66	200000	100	-	[119]
CQDs/ZIF-8	40000	43	30	[120]
N/CQDs/MIL-125	420	49	30	[121]
P/g-C_3N_4-MOF	600	74	30	[122]

MIL-125	500;750;1000	96	180	Present work
MIL-125-NH_2	500;750;1000	100	"	Present work
UiO-66	500;750;1000	92	"	Present work
UiO-66-NH_2	500;750;1000	100	"	Present work

3.2.3. Mechanistic insights into the photo-transformation and capture of NO_x in Metal-Organic Frameworks

Considering the performance of the studied MOF materials, a dual-function mechanism for the adsorption, transformation and immobilization of NOx species is proposed. First, at the adsorption stage in dark conditions, it is clear that the presence of basic amino functions in the porous frameworks plays a vital role in immobilizing NOx species both via acid–base interactions and even by nitrosation-like chemisorption. At this point, we have tried to observe by IR spectroscopy if these species are formed after the adsorption in dark conditions. Still, given the low-concentrated NOx atmosphere employed in our experiments, the variations in the IR spectra are negligible (Figure S16). The detection of oxidized nitrate/nitrite species was possible after repeating the light-triggered adsorption of NOx six times for the best-performing material (i.e. UiO-66-NH_2) (Figure 7a-b). The IR spectra of the post-use UiO-66-NH_2 show two additional bands at 827 (Figure 7b) and 1385 cm^{-1} (Figure 7a) and a small shoulder at 1350 cm^{-1} (Figure 7a). The two first IR signatures have been tentatively assigned as asymmetric stretching out-of-plane rocking vibrations of NO_2 motifs within weakly monodentate-coordinated nitrate anions. In parallel, the weak signal found at 1350 cm^{-1} can be assigned to the same vibration for free nitrate anions stabilized within the MOF.

This assignment has been done based on the broad bibliographic data for nitrate and nitrite species surface immobilization in different materials [123]. In brief, free nitrate has a D_{3h} symmetry and shows three IR-active vibrational modes related to ν_1 = out-of-plane rocking (~830 cm^{-1}), ν_2 = antisymmetric N–O stretching (~1350 cm^{-1}) and ν_3 = in-plane deformations (~719 cm^{-1}). When the nitrate anions coordinate to a surface in monodentate or bidentate modes, the D_{3h} symmetry is broken, and the ν_2 and ν_3 split into two different signals associated with the NO_2 fragment not linked to the surface, and the NO structure linked to the surface. The splitting and the shifting of these bands compared to the one observed for free nitrate anions depends on their coordination mode. The monodentate coordination of nitrates gives rise to a splitting/shifting of the asymmetric stretching from 1350 cm^{-1} in free nitrate to 1450 cm^{-1} and 1000 cm^{-1}. The IR signatures

of nitrate groups found in UiO-66-NH_2 point in that direction since one of the additional absorption bands is located close to 1385 cm^{-1}. This value is between the ones reported for free nitrate anions and monodentate-coordinated ones for cerium oxides. In addition, a weak signature is also observed at 1350 cm^{-1}, suggesting that free nitrates, more likely stabilized by electrostatic interaction with the amine groups of the UiO-66-NH_2 was also found after the photocatalytic-driven removal of NOx. Indeed, this band related to nitrate-free anions is one of the main ones seen in the IR spectra of the UiO-66-NH_2 material after immersing it into a sodium nitrate-saturated solution. This data has been employed as a reference when analyzing the post-operation IR fingerprints. In addition, we have confirmed that the UiO-66-NH_2 remains stable after the experiments and, thus, that the signals recorded by IR correspond to the nitrate immobilization into our porous photoactive framework (Figure 7c).

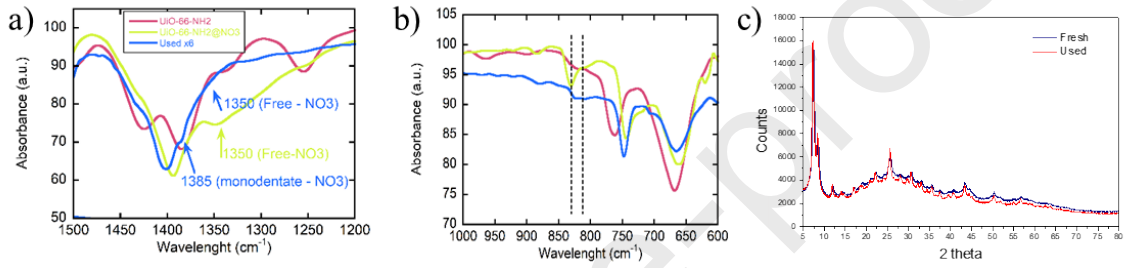

Figure 7 – (a-b) IR spectra of UiO-66-NH_2 before and after six NOx adsorption cycles under illumination. IR-spectra of the sample after immersing it in $NaNO_3$ saturated solution has been plotted as a reference. (c) XRD pattern of the UiO-66-N

By considering all the information, we can propose a three-step mechanism involving (I) the NOx adsorption, (II) their oxidation to nitrate species, and (III) their immobilization by coordinative bonds or weak interactions within the MOFs. First, in the adsorption step, the NOx is preferentially retained close to the basic amino groups of the framework, as illustrated in Figure 5A-B. As the IR after-operation does not show any band related to the fixation of the NOx via nitrosination, acid-base interactions between the NOx and the amine groups seem to be the most plausible adsorption mechanism (Figure 5B). Once illuminated, the light is harvested at the amino-functionalized linkers, electrons and hole pairs are generated and transported within the framework, and finally, the reactive oxygen species (ROS) are created once the $e^-/h\cdot$ pairs react with oxygen or water (Figure 5C). As reported for many oxidative photocatalysis processes before, ROS can be the main factor driving NOx's oxidation into nitrates. The question at this point is where the nitrite or nitrate species are stabilized within the MOF. Electrostatic interaction with amine or ammonium groups is one path that could stabilize close to free nitrate anions, showing an IR asymmetric vibration close to 1350 cm^{-1} (Figure 5D). In parallel, the migration and monodentate coordination of oxidized nitrate species close to the defective position of the titanium and zirconium oxo-clusters (Figure 5D) could explain the IR-band found at 1385 cm^{-1} in the experimental data.

3.3. Immobilization of the active materials in a porous membrane

In the circular economy of active materials, other factors come into play besides efficiency. Reutilization becomes a critical parameter to consider in the scope of sustainability and proper use of resources. As such, the immobilization of MIL-125-NH_2 into a composite membrane of two natural polymers, alginate and carrageenan, was a necessary next step to evaluate the ability of these active materials to operate in noxious environments.

Natural polymers are emerging as promising alternatives to synthetic polymers due to their biodegradability, biocompatibility, non-toxic nature, and low cost [124]. Unlike synthetic polymers, which often require toxic solvents for processing and are non-biodegradable, natural polymers are environmentally friendly and, therefore, interesting for the proposed application [125].

Preliminary morphological characterization of the membranes shows interconnected pores with a mean pore size of 159±20 µm (Figure 8a) and b)) with the dispersion of agglomerates of MOF within the polymeric substrate being highlighted in Figure 8c).

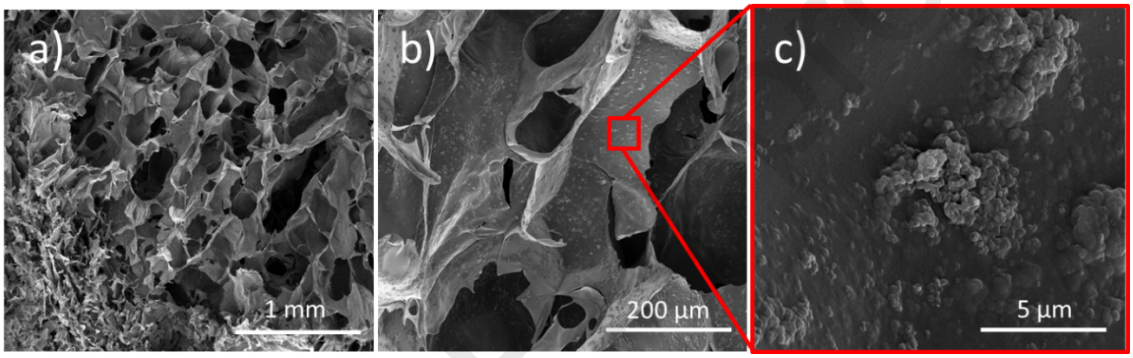

Figure 8 – Morphological characterization of the alginate/carrageenan (2% wt.) functionalized with 30 mg of MIL-125-NH_2.

Figure 9 presents the chemical, thermal and mechanical assessments of the produced membranes in their pristine form and functionalized with MIL-125-NH_2:

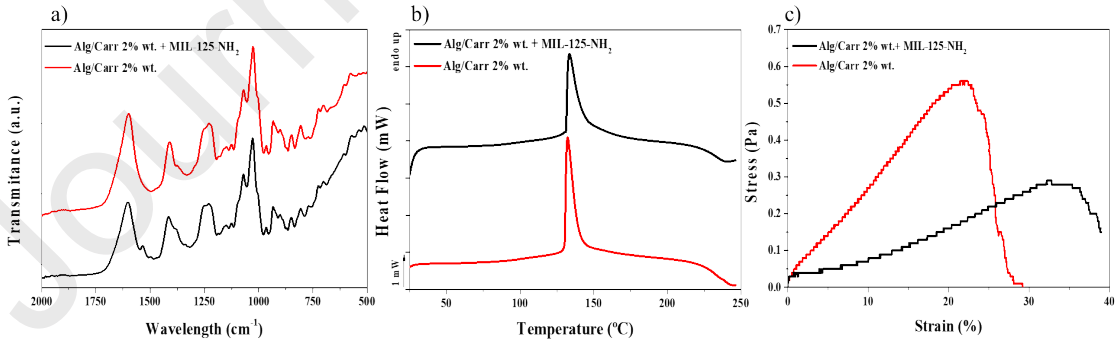

Figure 9 – Vibration bands (a), thermal (b), and mechanical (c) properties of the produced membranes.

The FTIR spectra (Figure 9a)) present three representative bands at 1596, 1409 and 1024 cm^{-1}, typical of Na-Alginate natural polymer. The first two bands correspond to metal-carboxylate vibrations, the first at 1596 cm^{-1} related to a strong asymmetric C=O stretching vibration and the one at 1409 cm^{-1} related to a weaker symmetric C=O stretching vibration. The band present at 1024 cm^{-1} corresponds to the C-O stretching vibrations. These results are consistent with those reported in the literature [126].

The carrageenan FTIR spectra usually reported in previous works show a well-defined band around 1240 cm^{-1}, related to the S=O bond of sulphate esters present in different types of carrageenan. However, a band can also be observed at 805 cm^{-1}. This band indicates the presence of sulphate ester in the 2-position of the anhydro-D-galactose residues, being this a typical band presented in ι-carrageenan like the one used for this membrane [127].

When both spectra are compared, the classic bands between 1700 to 1500 cm^{-1} and 1400 to 1300 cm^{-1}, corresponding to the carboxylates groups' asymmetrical and symmetrical vibrations of MIL-125-NH_2, are overlapped by the bands of the polymer due to a higher ratio of polymer in the membrane compared to the amount of the filler, except for the two small peaks at 1533 and 1494 cm^{-1}. Also, a slight difference in shape in the peaks ranging from 1450 to 1350 cm^{-1} can be ascribed to the presence of the MOF in the membrane. Finally, a minor feature in the peak around 1250 cm^{-1} is attributed to the C-N stretching vibrations of the amino groups.

It is observed that the thermal behaviour of the membranes is not modified when functionalized with the MIL-125-NH_2 (Figure 9b)). Adding the MOF to the pristine membrane does not induce significant changes to the peak corresponding to the Alginate/Carrageenan melting temperature at 133 ºC. As expected, this value is lower when compared to synthetic ones like PVDF [128]; however, it is still adequate for the application in question.

The mechanical behaviour of the two natural polymeric membranes (Figure 9c)) highlights an interesting observation when MIL-125-NH_2 is incorporated. The initial membrane exhibited a tensile strength of 2.07 MPa. However, with the addition of the MOF, the tensile strength experienced a reduction to 0.57 MPa. While this reduction is significant, it is worth noting that natural polymers generally exhibit lower mechanical strengths compared to synthetic polymers [129, 130]. This decrease can be attributed to different factors. Firstly, introducing the MOF might lead to microstructural modifications within the natural polymer matrix, influencing intermolecular interactions and, therefore, the load-bearing capacity of the membrane. Additionally, incorporating the MOF leads to membrane structure variations and stress concentration areas around the fillers [131, 132].

Figure 10 shows the results obtained for NO_x photocatalytic degradation by the alginate/carrageenan (2% wt.) membrane loaded with 15% (w/w) of MIL-125-NH_2. The membranes were subjected to three reutilization tests.

Journal Pre-proofs

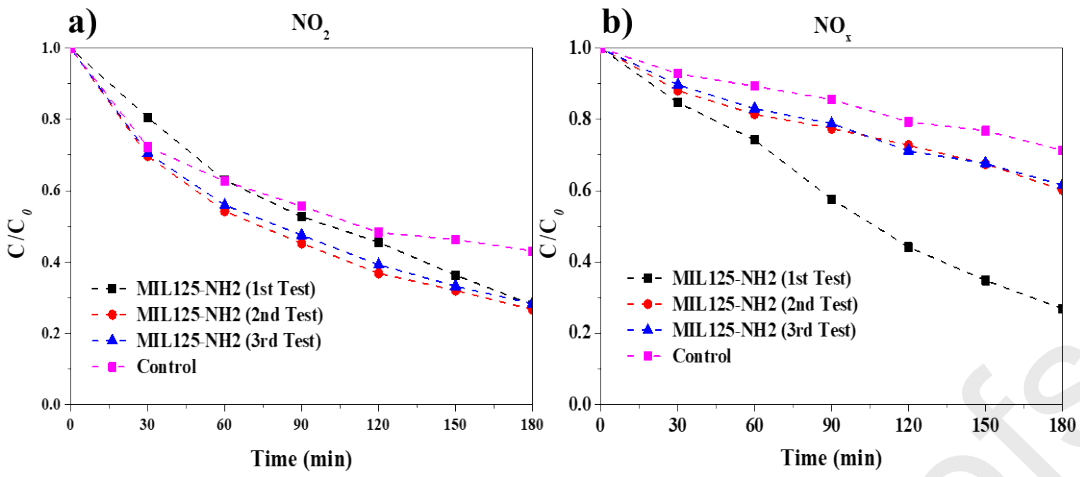

Figure 10 – Performance and reutilization efficiencies of MIL-125-NH_2 immobilized in a membrane of Alginate/Carrageenan.; a) NO_2; b) NO_x over time. Initial concentration = 1000 ppb under UV-light irradiation.

It is worth noting that the control membrane, which was a pristine membrane of Na-Alginate/Carrageenan (2% wt.), can reduce NO_x when irradiated by UV-A light. These properties can be ascribed to alginate and carrageenan reducing properties, which, inside the reactor, lead to reducing NO_x, mainly NO_2 [133]. Regarding material efficiency, the first test of the MIL-125-NH_2 shows an apparent degradation curve for the pollutant) with elevated degradation efficiencies for NO_x and NO_2, with nearly 80 and 70%, respectively (figure 10 a) and b)).

Concerning the reutilization of the membranes, a loss of around 30% can be observed after the first test for NO_x abatement (from 80% to 50%), while the percentage of NO_2 removal is maintained at about 70% for all three tests. Also, efficiency loss can be caused by the agglomerates observed in Figure 8b). The agglomeration of MOFs contributes to the loss of surface area and equally reduces the UV light irradiation of the MOF, leading to the observed efficiency loss.

In the literature, other systems are reported based on polymeric membranes with higher efficiencies in the remediation of NO_x, like the one of Majidi *et al*. [134], where synthetic (PVDF/PDMS) membranes were loaded with titanium dioxide nanoparticles to reach 100% efficiency. It is relevant to highlight that the setup used by these authors uses more energy to promote active contact between the gases and the material. Further, the setup herein presented only enables active material (passive contact), and only one of the surfaces of the membrane is exposed to UV radiation (light-harvesting). On the other hand, the present work presents an environmentally friendly approach for developing the membranes, which is a significant advantage and a real need in the scope of circular economy and sustainable approaches.

4. Conclusions

The alarming increase in air pollution levels poses significant risks to human health and the environment, exacerbating climate change. In this scope, four distinct chemical and thermally stable metal-organic frameworks, namely UiO-66, UiO-66-NH_2, MIL-125 and MIL-125-NH_2, were synthesized and applied for the light-driven adsorption, oxidation and immobilization of NO_x. Proved the crystallinity, particle size, defectiveness, and porosity of the studies MOF materials, NOx adsorption in dark conditions seems to be driven by the basic amino groups installed within the UiO-66-NH_2 and MIL-125-NH_2 frameworks. UiO-66 and MIL-125 present 92% and 96% degradation efficiencies, respectively, while adding -NH_2 groups double the adsorptive efficiency in dark conditions. When performing the experiments under UV-Vis irradiation, the overall efficiency of the process increases significantly, reaching nearly 100% degradation of NOx independently on the catalysts´ loading and NOx´s initial concentration. The stabilization of NOX oxidized species as free and monodentate coordinated anions has been confirmed by IR-spectroscopy of the post-use UiO-66-NH_2 sample.

Further, a straightforward immobilization strategy of the MIL-125-NH2 photoactive MOF into a highly porous air filter based on the blend of alginate and carrageenan polymers has been achieved. There is a noticeable decrease in efficiency of approximately 30% (from 80% to 50%) for NOx and a consistent removal of roughly 70% for NO_2 for MOF-based alginate and carrageenan membranes. It is important to note that the efficiency of the membrane is noticeable if it considers that the MOF is embedded in the polymeric system to a 10 % wt. of the membrane. Overall, the elimination of organic solvent usage through the utilization of natural polymers, namely alginate and carrageenan, along with novel materials functionalized with remarkable adsorptive and photocatalytic capabilities of MIL-125-NH_2, pave the way for a new way to tackle air remediation with sustainable approaches successfully.

Acknowledgements

The authors thank the Fundação para a Ciência e Tecnologia (FCT) for financial Support under the framework of Strategic Funding UIDB/04050/2020 and UID/FIS/04650/2020. J.T. and P. M. thank the FCT grant SFRH/BD/141642/2018 and contract 2020.02802.CEECIND, respectively. This study formed part of the Advanced Materials programme and was supported by MCIN with funding from European Union NextGenerationEU (PRTR-C17.I1) as well as by IKUR Strategy under the collaboration agreement between Ikerbasque Foundation and Fundación BCMaterials on behalf of the Department of Education of the Basque Government. The authors thank the financial support as well from the Spanish Agencia Estatal de Investigación (AEI) through EVOLMOF PID2021-122940OB-C31 (AEI/FEDER, UE) (including FEDER financial support), ENZYMOF (TED2021-130621B-C42), National, Fund for Scientific and Technological Development (FONDECYT REGULAR-ANID, 1220088), and Tailing32Green-ERAMIN projects. The MSCA-RISE-2017 (No 778412) INDESMOF HORIZON-MSCA-2022-SE-01-01 SELFAQUASENS (101131379) which received funding from the European Union's Horizon 2020 and Horizon Europe research and innovation programmes, are also acknowledged.

706

707

Journal Pre-proofs

Bibliography

[1] Resolution Adopted by the General Assembly on 25 September 2015, Sustainable Development Goals (2019) 333-374.

[2] M.-E. Héroux, H.R. Anderson, R. Atkinson, B. Brunekreef, A. Cohen, F. Forastiere, F. Hurley, K. Katsouyanni, D. Krewski, M. Krzyzanowski, N. Künzli, I. Mills, X. Querol, B. Ostro, H. Walton, Quantifying the health impacts of ambient air pollutants: recommendations of a WHO/Europe project, International Journal of Public Health 60(5) (2015) 619-627. https://doi.org/10.1007/s00038-015-0690-y.

[3] Z. Gholami, G. Luo, F. Gholami, F. Yang, Recent advances in selective catalytic reduction of NOx by carbon monoxide for flue gas cleaning process: a review, Catalysis Reviews 63(1) (2021) 68-119. https://doi.org/10.1080/01614940.2020.1753972.

[4] X. Sun, Y. Shi, W. Zhang, C. Li, Q. Zhao, J. Gao, X. Li, A new type Ni-MOF catalyst with high stability for selective catalytic reduction of NOx with NH3, Catalysis Communications 114 (2018) 104-108. https://doi.org/https://doi.org/10.1016/j.catcom.2018.06.012.

[5] T.-L. Chen, Y.-H. Chen, P.-C. Chiang, Enhanced performance on simultaneous removal of NOx-SO2-CO2 using a high-gravity rotating packed bed and alkaline wastes towards green process intensification, Chemical Engineering Journal 393 (2020) 124678. https://doi.org/https://doi.org/10.1016/j.cej.2020.124678.

[6] Z. Meng, C. Wang, X. Wang, Y. Chen, W. Wu, H. Li, Simultaneous removal of SO2 and NOx from flue gas using (NH4)2S2O3/steel slag slurry combined with ozone oxidation, Fuel 255 (2019) 115760. https://doi.org/https://doi.org/10.1016/j.fuel.2019.115760.

[7] H.P. Nguyen, M. Matsuoka, T.H. Kim, S.W. Lee, Iron(III)-based metal-organic frameworks as potential visible light-driven catalysts for the removal of NOx: A solution for urban air purification, Journal of Photochemistry and Photobiology A: Chemistry 367 (2018) 429-437. https://doi.org/https://doi.org/10.1016/j.jphotochem.2018.09.008.

[8] J. Ângelo, L. Andrade, L.M. Madeira, A. Mendes, An overview of photocatalysis phenomena applied to NOx abatement, Journal of Environmental Management 129 (2013) 522-539. https://doi.org/https://doi.org/10.1016/j.jenvman.2013.08.006.

[9] E.E.A. Eea, Air quality in europe-2019 report, Tech. rep. (2019).

[10] É. Laurent, L'Économie politique 69(1) (2016) 88-99.

[11] Y. Xie, H. Dai, H. Dong, Impacts of SO2 taxations and renewable energy development on CO2, NOx and SO2 emissions in Jing-Jin-Ji region, Journal of Cleaner Production 171 (2018) 1386-1395. https://doi.org/https://doi.org/10.1016/j.jclepro.2017.10.057.

[12] N.R. Jaegers, J.-K. Lai, Y. He, E. Walter, D.A. Dixon, M. Vasiliu, Y. Chen, C. Wang, M.Y. Hu, K.T. Mueller, I.E. Wachs, Y. Wang, J.Z. Hu, Mechanism by which Tungsten Oxide Promotes the Activity of Supported V2O5/TiO2 Catalysts for NOX Abatement: Structural Effects Revealed by 51V MAS NMR Spectroscopy, Angewandte Chemie International Edition 58(36) (2019) 12609-12616. https://doi.org/https://doi.org/10.1002/anie.201904503.

747 [13] Y. Shin, Y. Jung, C.P. Cho, Y.D. Pyo, J. Jang, G. Kim, T.M. Kim, NOx abatement and N2O
748 formation over urea-SCR systems with zeolite supported Fe and Cu catalysts in a nonroad
749 diesel engine, Chemical Engineering Journal 381 (2020) 122751.
750 https://doi.org/https://doi.org/10.1016/j.cej.2019.122751.

751 [14] M. Cortés-Reyes, M.Á. Larrubia, C. Herrera, L.J. Alemany, Influence of CO2 and H2O co-
752 feeding in the NOx abatement by SCR over an efficient Cu-CHA catalyst, Chemical Engineering
753 Science 201 (2019) 373-381. https://doi.org/https://doi.org/10.1016/j.ces.2019.02.031.

754 [15] B. Wei, W. Yang, J. Wang, H. Tan, S. Zhou, F. Wang, J. Ma, Study on reduction mechanism
755 of Fe2O3 by NH3 under SNCR condition, Fuel 255 (2019) 115814.
756 https://doi.org/https://doi.org/10.1016/j.fuel.2019.115814.

757 [16] J. Wang, B. Wei, X. Li, W. Yang, C. Zhang, I. Mian, H. Tan, F. Ma, Study on reduction
758 characteristics of Fe species in coal ash under SNCR condition, Fuel 277 (2020) 118231.
759 https://doi.org/https://doi.org/10.1016/j.fuel.2020.118231.

760 [17] V.T. Nguyen, D.B. Nguyen, I. Heo, Y.S. Mok, Plasma-Assisted Selective Catalytic Reduction
761 for Low-Temperature Removal of NOx and Soot Simulant, Catalysts 9(10) (2019).
762 https://doi.org/10.3390/catal9100853.

763 [18] T. Wang, X. Zhang, J. Liu, H. Liu, Y. Wang, B. Sun, Effects of temperature on NOx removal
764 with Mn-Cu/ZSM5 catalysts assisted by plasma, Applied Thermal Engineering 130 (2018) 1224-
765 1232. https://doi.org/https://doi.org/10.1016/j.applthermaleng.2017.11.113.

766 [19] B. Jiang, S. Zhao, Y. Wang, Y. Wenren, Z. Zhu, J. Harding, X. Zhang, X. Tu, X. Zhang, Plasma-
767 enhanced low temperature NH3-SCR of NOx over a Cu-Mn/SAPO-34 catalyst under oxygen-rich
768 conditions, Applied Catalysis B: Environmental 286 (2021) 119886.
769 https://doi.org/https://doi.org/10.1016/j.apcatb.2021.119886.

770 [20] X. Shi, F. Zhao, C. Cao, H. Zhang, X. Dang, T. Huang, Nitrogen oxide gas purification using
771 carbon in water as reducing reagent with the aid of microbial fuel cell, Journal of Hazardous
772 Materials 405 (2021) 124169. https://doi.org/https://doi.org/10.1016/j.jhazmat.2020.124169.

773 [21] A.K. Patel, Y.Y. Choi, S.J. Sim, Emerging prospects of mixotrophic microalgae: Way forward
774 to sustainable bioprocess for environmental remediation and cost-effective biofuels,
775 Bioresource Technology 300 (2020) 122741.
776 https://doi.org/https://doi.org/10.1016/j.biortech.2020.122741.

777 [22] K. Skalska, J.S. Miller, S. Ledakowicz, Trends in NOx abatement: A review, Science of The
778 Total Environment 408(19) (2010) 3976-3989.
779 https://doi.org/https://doi.org/10.1016/j.scitotenv.2010.06.001.

780 [23] H.-G. Kim, K.-W. Nam, Study of the Adsorption Possibility of SOx and NOx Using Porous
781 Diatomite Ceramic, Journal of Power System Engineering 25 (2021) 5-12.
782 https://doi.org/10.9726/kspse.2021.25.1.005.

783 [24] K. Silas, W.A.W.A.K. Ghani, T.S.Y. Choong, U. Rashid, Activated carbon monolith Co3O4
784 based catalyst: Synthesis, characterization and adsorption studies, Environmental Technology
785 & Innovation 12 (2018) 273-285. https://doi.org/https://doi.org/10.1016/j.eti.2018.10.008.

786 [25] M. Berger, H. Nouali, S. Dorge, D. Habermacher, E. Fiani, M. Vierling, M. Molière, C.
787 Schönnenbeck, J.-F. Brilhac, J. Patarin, Long-term activity of a CuO/SBA-15 type SOx adsorbent:

788 Impact of the regeneration step, Chemical Engineering Journal 347 (2018) 202-213.
789 https://doi.org/https://doi.org/10.1016/j.cej.2018.04.066.

790 [26] H.P. Nguyen, S. Palma Del Valle, O. Marie, NOx adsorption on K and Ba loaded on zirconia-
791 titania NSR catalysts: A comparative study by in situ and operando IR spectroscopy, Applied
792 Catalysis B: Environmental 231 (2018) 391-399.
793 https://doi.org/https://doi.org/10.1016/j.apcatb.2018.03.002.

794 [27] D.A. Gkika, A.C. Mitropoulos, G.Z. Kyzas, Why reuse spent adsorbents? The latest
795 challenges and limitations, Science of The Total Environment 822 (2022) 153612.
796 https://doi.org/https://doi.org/10.1016/j.scitotenv.2022.153612.

797 [28] A.A. Abdulrasheed, A.A. Jalil, S. Triwahyono, M.A.A. Zaini, Y. Gambo, M. Ibrahim, Surface
798 modification of activated carbon for adsorption of SO2 and NOX: A review of existing and
799 emerging technologies, Renewable and Sustainable Energy Reviews 94 (2018) 1067-1085.
800 https://doi.org/https://doi.org/10.1016/j.rser.2018.07.011.

801 [29] Q. Li, Y. Hou, N. Xiang, Y. Liu, Z. Huang, A new insight into the promotional effect of
802 nitrogen-doping in activated carbon for selective catalytic reduction of NOX with NH3, Science
803 of The Total Environment 740 (2020) 140158.
804 https://doi.org/https://doi.org/10.1016/j.scitotenv.2020.140158.

805 [30] I. Ghouma, M. Jeguirim, U. Sager, L. Limousy, S. Bennici, E. Däuber, C. Asbach, R. Ligotski,
806 F. Schmidt, A. Ouederni, The Potential of Activated Carbon Made of Agro-Industrial Residues in
807 NOx Immissions Abatement, Energies 10(10) (2017). https://doi.org/10.3390/en10101508.

808 [31] H. Yi, C. Ma, X. Tang, S. Zhao, K. Yang, Z. Sani, L. Song, X. Zhang, W. Han, Synthesis of
809 MgO@CeO2-MnOx core shell structural adsorbent and its application in reducing the
810 competitive adsorption of SO2 and NOx in coal-fired flue gas, Chemical Engineering Journal
811 372 (2019) 129-140. https://doi.org/https://doi.org/10.1016/j.cej.2019.04.120.

812 [32] K. Erme, I. Jõgi, Metal Oxides as Catalysts and Adsorbents in Ozone Oxidation of NOx,
813 Environmental Science & Technology 53(9) (2019) 5266-5271.
814 https://doi.org/10.1021/acs.est.8b07307.

815 [33] Q. Xu, D. Liu, C. Wang, W. Zhan, Y. Guo, Y. Guo, L. Wang, Q. Ke, M.N. Ha, Sb-Containing
816 Metal Oxide Catalysts for the Selective Catalytic Reduction of NOx with NH3, Catalysts 10(10)
817 (2020). https://doi.org/10.3390/catal10101154.

818 [34] Z. Fan, J.-W. Shi, C. Niu, B. Wang, C. He, Y. Cheng, The insight into the role of Al2O3 in
819 promoting the SO2 tolerance of MnOx for low-temperature selective catalytic reduction of
820 NOx with NH3, Chemical Engineering Journal 398 (2020) 125572.
821 https://doi.org/https://doi.org/10.1016/j.cej.2020.125572.

822 [35] J.Y. Lim, K. Kim, E.Y. Kim, J.W. Han, Density functional theory study of NOx adsorption on
823 alkaline earth metal oxide and transition metal surfaces, Korean Journal of Chemical
824 Engineering 36(8) (2019) 1258-1266. https://doi.org/10.1007/s11814-019-0324-9.

825 [36] D. Mei, F. Gao, J. Szanyi, Y. Wang, Mechanistic insight into the passive NOx adsorption in
826 the highly dispersed Pd/HBEA zeolite, Applied Catalysis A: General 569 (2019) 181-189.
827 https://doi.org/https://doi.org/10.1016/j.apcata.2018.10.037.

[37] H.I. Hamoud, V. Valtchev, M. Daturi, Selective catalytic reduction of NOx over Cu- and Fe-exchanged zeolites and their mechanical mixture, Applied Catalysis B: Environmental 250 (2019) 419-428. https://doi.org/https://doi.org/10.1016/j.apcatb.2019.02.022.

[38] E. Bello, V.J. Margarit, E.M. Gallego, F. Schuetze, C. Hengst, A. Corma, M. Moliner, Deactivation and regeneration studies on Pd-containing medium pore zeolites as passive NOx adsorbers (PNAs) in cold-start applications, Microporous and Mesoporous Materials 302 (2020) 110222. https://doi.org/https://doi.org/10.1016/j.micromeso.2020.110222.

[39] S. Mohan, P. Dinesha, S. Kumar, NOx reduction behaviour in copper zeolite catalysts for ammonia SCR systems: A review, Chemical Engineering Journal 384 (2020) 123253. https://doi.org/https://doi.org/10.1016/j.cej.2019.123253.

[40] J.O. Ighalo, F.O. Omoarukhe, V.E. Ojukwu, K.O. Iwuozor, C.A. Igwegbe, Cost of adsorbent preparation and usage in wastewater treatment: A review, Cleaner Chemical Engineering 3 (2022) 100042. https://doi.org/https://doi.org/10.1016/j.clce.2022.100042.

[41] V.-H. Nguyen, B.-S. Nguyen, C.-W. Huang, T.-T. Le, C.C. Nguyen, T.T. Nhi Le, D. Heo, Q.V. Ly, Q.T. Trinh, M. Shokouhimehr, C. Xia, S.S. Lam, D.-V.N. Vo, S.Y. Kim, Q.V. Le, Photocatalytic NOx abatement: Recent advances and emerging trends in the development of photocatalysts, Journal of Cleaner Production 270 (2020) 121912. https://doi.org/https://doi.org/10.1016/j.jclepro.2020.121912.

[42] V. Khanal, N.O. Balayeva, C. Günnemann, Z. Mamiyev, R. Dillert, D.W. Bahnemann, V. Subramanian, Photocatalytic NOx removal using tantalum oxide nanoparticles: A benign pathway, Applied Catalysis B: Environmental 291 (2021) 119974. https://doi.org/https://doi.org/10.1016/j.apcatb.2021.119974.

[43] M. Nagalakshmi, C. Karthikeyan, N. Anusuya, C. Brundha, M.J. Basu, S. Karuppuchamy, Synthesis of TiO2 nanofiber for photocatalytic and antibacterial applications, Journal of Materials Science: Materials in Electronics 28(21) (2017) 15915-15920. https://doi.org/10.1007/s10854-017-7487-0.

[44] M.R. Al-Mamun, S. Kader, M.S. Islam, M.Z.H. Khan, Photocatalytic activity improvement and application of UV-TiO2 photocatalysis in textile wastewater treatment: A review, Journal of Environmental Chemical Engineering 7(5) (2019) 103248. https://doi.org/https://doi.org/10.1016/j.jece.2019.103248.

[45] A. Gupta, J.R. Saurav, S. Bhattacharya, Solar light based degradation of organic pollutants using ZnO nanobrushes for water filtration, RSC Advances 5(87) (2015) 71472-71481. https://doi.org/10.1039/C5RA10456D.

[46] K. Ozturk, N.K. Bakirhan, S.A. Ozkan, B. Uslu, Effect of Catalytically Active Zinc Oxide–Carbon Nanotube Composite on Sensitive Assay of Desloratadine Metabolite, Electroanalysis 32(1) (2020) 50-58. https://doi.org/https://doi.org/10.1002/elan.201900193.

[47] Y. Huang, D. Zhu, Q. Zhang, Y. Zhang, J.-j. Cao, Z. Shen, W. Ho, S.C. Lee, Synthesis of a Bi2O2CO3/ZnFe2O4 heterojunction with enhanced photocatalytic activity for visible light irradiation-induced NO removal, Applied Catalysis B: Environmental 234 (2018) 70-78. https://doi.org/https://doi.org/10.1016/j.apcatb.2018.04.039.

[48] G. Zhu, S. Li, J. Gao, F. Zhang, C. Liu, Q. Wang, M. Hojamberdiev, Constructing a 2D/2D Bi2O2CO3/Bi4O5Br2 heterostructure as a direct Z-scheme photocatalyst with enhanced

photocatalytic activity for NOx removal, Applied Surface Science 493 (2019) 913-925. https://doi.org/https://doi.org/10.1016/j.apsusc.2019.07.119.

[49] M. Chen, Y. Huang, J. Yao, J.-j. Cao, Y. Liu, Visible-light-driven N-(BiO)2CO3/Graphene oxide composites with improved photocatalytic activity and selectivity for NOx removal, Applied Surface Science 430 (2018) 137-144. https://doi.org/https://doi.org/10.1016/j.apsusc.2017.06.056.

[50] Z. Gu, B. Zhang, Y. Asakura, S. Tsukuda, H. Kato, M. Kakihana, S. Yin, Alkali-assisted hydrothermal preparation of g-C3N4/rGO nanocomposites with highly enhanced photocatalytic NOx removal activity, Applied Surface Science 521 (2020) 146213. https://doi.org/https://doi.org/10.1016/j.apsusc.2020.146213.

[51] E. Falletta, C.L. Bianchi, F. Morazzoni, A. Polissi, F. Di Vincenzo, I.R. Bellobono, Tungsten Trioxide and Its TiO2 Mixed Composites for the Photocatalytic Degradation of NOx and Bacteria (Escherichia coli) Inactivation, Catalysts 12(8) (2022). https://doi.org/10.3390/catal12080822.

[52] H. Khan, M. Gar Alalm, M. Lalonde-Lavoie, M.F. Ordonez, M. Sartirana, A. Giordana, G. Cerrato, C.L. Bianchi, D.C. Boffito, Photocatalytic degradation of NOx and ethanol in the gas phase by spray dried Ce-TiO2, Journal of Environmental Chemical Engineering 9(6) (2021) 106813. https://doi.org/https://doi.org/10.1016/j.jece.2021.106813.

[53] J. Lin, W. Ho, X. Qin, C.-F. Leung, V.K.-M. Au, S.-c. Lee, Metal–Organic Frameworks for NOx Adsorption and Their Applications in Separation, Sensing, Catalysis, and Biology, Small 18(13) (2022) 2105484. https://doi.org/https://doi.org/10.1002/smll.202105484.

[54] S. Yuan, L. Feng, K. Wang, J. Pang, M. Bosch, C. Lollar, Y. Sun, J. Qin, X. Yang, P. Zhang, Q. Wang, L. Zou, Y. Zhang, L. Zhang, Y. Fang, J. Li, H.-C. Zhou, Stable Metal–Organic Frameworks: Design, Synthesis, and Applications, Advanced Materials 30(37) (2018) 1704303. https://doi.org/https://doi.org/10.1002/adma.201704303.

[55] P. Kumar, K.-H. Kim, S. Rarotra, L. Ge, G. Lisak, The advanced sensing systems for NOx based on metal-organic frameworks: Applications and future opportunities, TrAC Trends in Analytical Chemistry 122 (2020) 115730. https://doi.org/https://doi.org/10.1016/j.trac.2019.115730.

[56] f. Tang, Y. Zhai, S. Li, L. Li, X. Wei, J. Hu, L. Ruan, Z. Zhang, Study on NO selective adsorption performance of Rh/MOF-177, 2020. https://doi.org/10.22541/au.160418532.27740129/v1.

[57] D.F. Sava Gallis, D.J. Vogel, G.A. Vincent, J.M. Rimsza, T.M. Nenoff, NOx Adsorption and Optical Detection in Rare Earth Metal–Organic Frameworks, ACS Applied Materials & Interfaces 11(46) (2019) 43270-43277. https://doi.org/10.1021/acsami.9b16470.

[58] Y. Zhang, S. Yuan, X. Feng, H. Li, J. Zhou, B. Wang, Preparation of Nanofibrous Metal–Organic Framework Filters for Efficient Air Pollution Control, Journal of the American Chemical Society 138(18) (2016) 5785-5788. https://doi.org/10.1021/jacs.6b02553.

[59] Y. Bian, R. Wang, S. Wang, C. Yao, W. Ren, C. Chen, L. Zhang, Metal–organic framework-based nanofiber filters for effective indoor air quality control, Journal of Materials Chemistry A 6(32) (2018) 15807-15814. https://doi.org/10.1039/C8TA04539A.

911 [60] Q. Wang, Q. Gao, A.M. Al-Enizi, A. Nafady, S. Ma, Recent advances in MOF-based
912 photocatalysis: environmental remediation under visible light, Inorganic Chemistry Frontiers
913 7(2) (2020) 300-339. https://doi.org/10.1039/C9QI01120J.

914 [61] Q. Pang, B. Tu, Q. Li, Metal–organic frameworks with multicomponents in order,
915 Coordination Chemistry Reviews 388 (2019) 107-125.
916 https://doi.org/https://doi.org/10.1016/j.ccr.2019.02.022.

917 [62] E.D. Bloch, W.L. Queen, S. Chavan, P.S. Wheatley, J.M. Zadrozny, R. Morris, C.M. Brown, C.
918 Lamberti, S. Bordiga, J.R. Long, Gradual Release of Strongly Bound Nitric Oxide from
919 Fe2(NO)2(dobdc), Journal of the American Chemical Society 137(10) (2015) 3466-3469.
920 https://doi.org/10.1021/ja5132243.

921 [63] J.B. Decoste, G.W. Peterson, M.W. Smith, C.A. Stone, C.R. Willis, Enhanced Stability of Cu-
922 BTC MOF via Perfluorohexane Plasma-Enhanced Chemical Vapor Deposition, Journal of the
923 American Chemical Society 134(3) (2012) 1486-1489. https://doi.org/10.1021/ja211182m.

924 [64] B. Lin, A. Wang, Y. Guo, Y. Ding, Y. Guo, L. Wang, W. Zhan, F. Gao, Ambient Temperature
925 NO Adsorber Derived from Pyrolysis of Co-MOF(ZIF-67), ACS Omega 4(5) (2019) 9542-9551.
926 https://doi.org/10.1021/acsomega.9b00763.

927 [65] L. Chen, F. Yu, X. Shen, C. Duan, N-CND modified NH2-UiO-66 for photocatalytic CO2
928 conversion under visible light by a photo-induced electron transfer process, Chemical
929 Communications 55(33) (2019) 4845-4848. https://doi.org/10.1039/C9CC02193K.

930 [66] M. Aghajanzadeh, M. Zamani, H. Molavi, H. Khieri Manjili, H. Danafar, A. Shojaei,
931 Preparation of Metal–Organic Frameworks UiO-66 for Adsorptive Removal of Methotrexate
932 from Aqueous Solution, Journal of Inorganic and Organometallic Polymers and Materials 28(1)
933 (2018) 177-186. https://doi.org/10.1007/s10904-017-0709-3.

934 [67] M. Sohail, Y.-N. Yun, E. Lee, S.K. Kim, K. Cho, J.-N. Kim, T.W. Kim, J.-H. Moon, H. Kim,
935 Synthesis of Highly Crystalline NH2-MIL-125 (Ti) with S-Shaped Water Isotherms for Adsorption
936 Heat Transformation, Crystal Growth & Design 17(3) (2017) 1208-1213.
937 https://doi.org/10.1021/acs.cgd.6b01597.

938 [68] P. G. Saiz, A. Valverde, B. Gonzalez-Navarrete, M. Rosales, Y.M. Quintero, A. Fidalgo-
939 Marijuan, J. Orive, A. Reizabal, E.S. Larrea, M.I. Arriortua, S. Lanceros-Méndez, A. García, R.
940 Fernández de Luis, Modulation of the Bifunctional CrVI to CrIII Photoreduction and Adsorption
941 Capacity in ZrIV and TiIV Benchmark Metal-Organic Frameworks, Catalysts 11(1) (2021).
942 https://doi.org/10.3390/catal11010051.

943 [69] K.C. Kim, T.-U. Yoon, Y.-S. Bae, Applicability of using CO2 adsorption isotherms to
944 determine BET surface areas of microporous materials, Microporous and Mesoporous
945 Materials 224 (2016) 294-301.
946 https://doi.org/https://doi.org/10.1016/j.micromeso.2016.01.003.

947 [70] Q. Li, Y. Li, X. Ma, Q. Du, K. Sui, D. Wang, C. Wang, H. Li, Y. Xia, Filtration and adsorption
948 properties of porous calcium alginate membrane for methylene blue removal from water,
949 Chemical Engineering Journal 316 (2017) 623-630.
950 https://doi.org/https://doi.org/10.1016/j.cej.2017.01.098.

951 [71] S.-J. Lee, J.L. Mancuso, K.N. Le, C.D. Malliakas, Y.-S. Bae, C.H. Hendon, T. Islamoglu, O.K.
952 Farha, Time-Resolved in Situ Polymorphic Transformation from One 12-Connected Zr-MOF to

Another, ACS Materials Letters 2(5) (2020) 499-504.
https://doi.org/10.1021/acsmaterialslett.0c00012.

[72] M.A. Nasalevich, R. Becker, E.V. Ramos-Fernandez, S. Castellanos, S.L. Veber, M.V. Fedin, F. Kapteijn, J.N.H. Reek, J.I. van der Vlugt, J. Gascon, Co@NH2-MIL-125(Ti): cobaloxime-derived metal–organic framework-based composite for light-driven H2 production, Energy & Environmental Science 8(1) (2015) 364-375. https://doi.org/10.1039/C4EE02853H.

[73] C.L. Luu, T.T. Van Nguyen, T. Nguyen, T.C. Hoang, Synthesis, characterization and adsorption ability of UiO-66-NH2, Advances in Natural Sciences: Nanoscience and Nanotechnology 6(2) (2015) 025004.

[74] G.Y. Shangkum, P. Chammingkwan, D.X. Trinh, T. Taniike, Design of a Semi-Continuous Selective Layer Based on Deposition of UiO-66 Nanoparticles for Nanofiltration, Membranes 8(4) (2018). https://doi.org/10.3390/membranes8040129.

[75] Y. Han, M. Liu, K. Li, Y. Zuo, Y. Wei, S. Xu, G. Zhang, C. Song, Z. Zhang, X. Guo, Facile synthesis of morphology and size-controlled zirconium metal–organic framework UiO-66: the role of hydrofluoric acid in crystallization, CrystEngComm 17(33) (2015) 6434-6440. https://doi.org/10.1039/C5CE00729A.

[76] M. Kandiah, S. Usseglio, S. Svelle, U. Olsbye, K.P. Lillerud, M. Tilset, Post-synthetic modification of the metal–organic framework compound UiO-66, Journal of Materials Chemistry 20(44) (2010) 9848-9851. https://doi.org/10.1039/C0JM02416C.

[77] I.D. Ivanchikova, J.S. Lee, N.V. Maksimchuk, A.N. Shmakov, Y.A. Chesalov, A.B. Ayupov, Y.K. Hwang, C.-H. Jun, J.-S. Chang, O.A. Kholdeeva, Highly Selective H2O2-Based Oxidation of Alkylphenols to p-Benzoquinones Over MIL-125 Metal–Organic Frameworks, European Journal of Inorganic Chemistry 2014(1) (2014) 132-139.
https://doi.org/https://doi.org/10.1002/ejic.201301098.

[78] M. Dan-Hardi, C. Serre, T. Frot, L. Rozes, G. Maurin, C. Sanchez, G. Férey, A New Photoactive Crystalline Highly Porous Titanium(IV) Dicarboxylate, Journal of the American Chemical Society 131(31) (2009) 10857-10859. https://doi.org/10.1021/ja903726m.

[79] R.S. Salama, E.-S.M. El-Sayed, S.M. El-Bahy, F.S. Awad, Silver nanoparticles supported on UiO-66 (Zr): As an efficient and recyclable heterogeneous catalyst and efficient adsorbent for removal of indigo carmine, Colloids and Surfaces A: Physicochemical and Engineering Aspects 626 (2021) 127089. https://doi.org/https://doi.org/10.1016/j.colsurfa.2021.127089.

[80] C.L. Luu, T.T.V. Nguyen, T. Nguyen, T.C. Hoang, Synthesis, characterization and adsorption ability of UiO-66-NH 2, Advances in Natural Sciences: Nanoscience and Nanotechnology 6(2) (2015) 025004. https://doi.org/10.1088/2043-6262/6/2/025004.

[81] N.D. McNamara, G.T. Neumann, E.T. Masko, J.A. Urban, J.C. Hicks, Catalytic performance and stability of (V) MIL-47 and (Ti) MIL-125 in the oxidative desulfurization of heterocyclic aromatic sulfur compounds, Journal of Catalysis 305 (2013) 217-226.
https://doi.org/https://doi.org/10.1016/j.jcat.2013.05.021.

[82] N.J. Castellanos, Z. Martinez Rojas, H.A. Camargo, S. Biswas, G. Granados-Oliveros, Congo red decomposition by photocatalytic formation of hydroxyl radicals (·OH) using titanium metal–organic frameworks, Transition Metal Chemistry 44(1) (2019) 77-87.
https://doi.org/10.1007/s11243-018-0271-z.

[83] D. Sun, W. Liu, M. Qiu, Y. Zhang, Z. Li, Introduction of a mediator for enhancing photocatalytic performance via post-synthetic metal exchange in metal–organic frameworks (MOFs), Chemical Communications 51(11) (2015) 2056-2059. https://doi.org/10.1039/C4CC09407G.

[84] S.-N. Kim, J. Kim, H.-Y. Kim, H.-Y. Cho, W.-S. Ahn, Adsorption/catalytic properties of MIL-125 and NH2-MIL-125, Catalysis Today 204 (2013) 85-93. https://doi.org/https://doi.org/10.1016/j.cattod.2012.08.014.

[85] Y. He, S. Luo, X. Hu, Y. Cheng, Y. Huang, S. Chen, M. Fu, Y. Jia, X. Liu, NH2-MIL-125(Ti) encapsulated with in situ-formed carbon nanodots with up-conversion effect for improving photocatalytic NO removal and H2 evolution, Chemical Engineering Journal 420 (2021) 127643. https://doi.org/https://doi.org/10.1016/j.cej.2020.127643.

[86] G.W. Peterson, J.J. Mahle, J.B. DeCoste, W.O. Gordon, J.A. Rossin, Extraordinary NO2 Removal by the Metal–Organic Framework UiO-66-NH2, Angewandte Chemie International Edition 55(21) (2016) 6235-6238. https://doi.org/https://doi.org/10.1002/anie.201601782.

[87] M. Bertmer, Chapter One - Solid-state NMR of small molecule adsorption in metal–organic frameworks (MOFs), in: R. Atta ur (Ed.), Annual Reports on NMR Spectroscopy, Academic Press2020, pp. 1-64. https://doi.org/https://doi.org/10.1016/bs.arnmr.2020.07.003.

[88] A.M. Ebrahim, B. Levasseur, T.J. Bandosz, Interactions of NO2 with Zr-Based MOF: Effects of the Size of Organic Linkers on NO2 Adsorption at Ambient Conditions, Langmuir 29(1) (2013) 168-174. https://doi.org/10.1021/la302869m.

[89] X. Han, S. Yang, M. Schröder, Porous metal–organic frameworks as emerging sorbents for clean air, Nature Reviews Chemistry 3(2) (2019) 108-118. https://doi.org/10.1038/s41570-019-0073-7.

[90] X. Zhang, I. da Silva, H.G.W. Godfrey, S.K. Callear, S.A. Sapchenko, Y. Cheng, I. Vitórica-Yrezábal, M.D. Frogley, G. Cinque, C.C. Tang, C. Giacobbe, C. Dejoie, S. Rudić, A.J. Ramirez-Cuesta, M.A. Denecke, S. Yang, M. Schröder, Confinement of Iodine Molecules into Triple-Helical Chains within Robust Metal–Organic Frameworks, Journal of the American Chemical Society 139(45) (2017) 16289-16296. https://doi.org/10.1021/jacs.7b08748.

[91] Q. Min Wang, D. Shen, M. Bülow, M. Ling Lau, S. Deng, F.R. Fitch, N.O. Lemcoff, J. Semanscin, Metallo-organic molecular sieve for gas separation and purification, Microporous and Mesoporous Materials 55(2) (2002) 217-230. https://doi.org/https://doi.org/10.1016/S1387-1811(02)00405-5.

[92] A.R. Millward, O.M. Yaghi, Metal−Organic Frameworks with Exceptionally High Capacity for Storage of Carbon Dioxide at Room Temperature, Journal of the American Chemical Society 127(51) (2005) 17998-17999. https://doi.org/10.1021/ja0570032.

[93] I. Ahmed, S.H. Jhung, Adsorptive desulfurization and denitrogenation using metal-organic frameworks, Journal of Hazardous Materials 301 (2016) 259-276. https://doi.org/https://doi.org/10.1016/j.jhazmat.2015.08.045.

[94] A.C. McKinlay, J.F. Eubank, S. Wuttke, B. Xiao, P.S. Wheatley, P. Bazin, J.C. Lavalley, M. Daturi, A. Vimont, G. De Weireld, P. Horcajada, C. Serre, R.E. Morris, Nitric Oxide Adsorption and Delivery in Flexible MIL-88(Fe) Metal–Organic Frameworks, Chemistry of Materials 25(9) (2013) 1592-1599. https://doi.org/10.1021/cm304037x.

[95] A.H. Khan, K. Peikert, F. Hoffmann, M. Fröba, M. Bertmer, Nitric Oxide Adsorption in Cu3btc2-Type MOFs—Physisorption and Chemisorption as NONOates, The Journal of Physical Chemistry C 123(7) (2019) 4299-4307. https://doi.org/10.1021/acs.jpcc.8b11919.

[96] J.E. Mondloch, W. Bury, D. Fairen-Jimenez, S. Kwon, E.J. DeMarco, M.H. Weston, A.A. Sarjeant, S.T. Nguyen, P.C. Stair, R.Q. Snurr, O.K. Farha, J.T. Hupp, Vapor-Phase Metalation by Atomic Layer Deposition in a Metal–Organic Framework, Journal of the American Chemical Society 135(28) (2013) 10294-10297. https://doi.org/10.1021/ja4050828.

[97] J.H. Cavka, S. Jakobsen, U. Olsbye, N. Guillou, C. Lamberti, S. Bordiga, K.P. Lillerud, A New Zirconium Inorganic Building Brick Forming Metal Organic Frameworks with Exceptional Stability, Journal of the American Chemical Society 130(42) (2008) 13850-13851. https://doi.org/10.1021/ja8057953.

[98] L. Li, R.-B. Lin, R. Krishna, H. Li, S. Xiang, H. Wu, J. Li, W. Zhou, B. Chen, Ethane/ethylene separation in a metal-organic framework with iron-peroxo sites, Science 362(6413) (2018) 443-446. https://doi.org/10.1126/science.aat0586.

[99] S. Shang, C. Yang, C. Wang, J. Qin, Y. Li, Q. Gu, J. Shang, Transition-Metal-Containing Porphyrin Metal–Organic Frameworks as π-Backbonding Adsorbents for NO2 Removal, Angewandte Chemie International Edition 59(44) (2020) 19680-19683. https://doi.org/https://doi.org/10.1002/anie.202007054.

[100] B. Levasseur, C. Petit, T.J. Bandosz, Reactive Adsorption of NO2 on Copper-Based Metal−Organic Framework and Graphite Oxide/Metal−Organic Framework Composites, ACS Applied Materials & Interfaces 2(12) (2010) 3606-3613. https://doi.org/10.1021/am100790v.

[101] F. Millange, C. Serre, G. Férey, Synthesis, structure determination and properties of MIL-53as and MIL-53ht: the first Criii hybrid inorganic–organic microporous solids: Criii(OH)·{O2C–C6H4–CO2}·{HO2C–C6H4–CO2H}x, Chemical Communications (8) (2002) 822-823. https://doi.org/10.1039/B201381A.

[102] J.B. DeCoste, T.J. Demasky, M.J. Katz, O.K. Farha, J.T. Hupp, A UiO-66 analogue with uncoordinated carboxylic acids for the broad-spectrum removal of toxic chemicals, New Journal of Chemistry 39(4) (2015) 2396-2399. https://doi.org/10.1039/C4NJ02093F.

[103] A.M. Ebrahim, T.J. Bandosz, Ce(III) Doped Zr-Based MOFs as Excellent NO2 Adsorbents at Ambient Conditions, ACS Applied Materials & Interfaces 5(21) (2013) 10565-10573. https://doi.org/10.1021/am402305u.

[104] A.M. Ebrahim, T.J. Bandosz, Effect of amine modification on the properties of zirconium–carboxylic acid based materials and their applications as NO2 adsorbents at ambient conditions, Microporous and Mesoporous Materials 188 (2014) 149-162. https://doi.org/https://doi.org/10.1016/j.micromeso.2014.01.009.

[105] X. Han, Y. Hong, Y. Ma, W. Lu, J. Li, L. Lin, A.M. Sheveleva, F. Tuna, E.J.L. McInnes, C. Dejoie, J. Sun, S. Yang, M. Schröder, Adsorption of Nitrogen Dioxide in a Redox-Active Vanadium Metal–Organic Framework Material, Journal of the American Chemical Society 142(36) (2020) 15235-15239. https://doi.org/10.1021/jacs.0c06414.

[106] A. Nisar, M. Saeed, M. Usman, M. Muneer, M. Adeel, I. Khan, J. Akhtar, Kinetic modeling of ZnO-rGO catalyzed degradation of methylene blue, International Journal of Chemical Kinetics 52(10) (2020) 645-654. https://doi.org/https://doi.org/10.1002/kin.21389.

[107] A. Houas, H. Lachheb, M. Ksibi, E. Elaloui, C. Guillard, J.-M. Herrmann, Photocatalytic degradation pathway of methylene blue in water, Applied Catalysis B: Environmental 31(2) (2001) 145-157. https://doi.org/https://doi.org/10.1016/S0926-3373(00)00276-9.

[108] I.K. Konstantinou, T.A. Albanis, TiO2-assisted photocatalytic degradation of azo dyes in aqueous solution: kinetic and mechanistic investigations: A review, Applied Catalysis B: Environmental 49(1) (2004) 1-14. https://doi.org/https://doi.org/10.1016/j.apcatb.2003.11.010.

[109] T. Sauer, G. Cesconeto Neto, H.J. José, R.F.P.M. Moreira, Kinetics of photocatalytic degradation of reactive dyes in a TiO2 slurry reactor, Journal of Photochemistry and Photobiology A: Chemistry 149(1) (2002) 147-154. https://doi.org/https://doi.org/10.1016/S1010-6030(02)00015-1.

[110] A. Mahmood, X. Wang, X. Xie, J. Sun, Degradation behavior of mixed and isolated aromatic ring containing VOCs: Langmuir-Hinshelwood kinetics, photodegradation, in-situ FTIR and DFT studies, Journal of Environmental Chemical Engineering 9(2) (2021) 105069. https://doi.org/https://doi.org/10.1016/j.jece.2021.105069.

[111] H. Yang, G. Li, T. An, Y. Gao, J. Fu, Photocatalytic degradation kinetics and mechanism of environmental pharmaceuticals in aqueous suspension of TiO2: A case of sulfa drugs, Catalysis Today 153(3) (2010) 200-207. https://doi.org/https://doi.org/10.1016/j.cattod.2010.02.068.

[112] H.A. Hamad, W.A. Sadik, M.M. Abd El-latif, A.B. Kashyout, M.Y. Feteha, Photocatalytic parameters and kinetic study for degradation of dichlorophenol-indophenol (DCPIP) dye using highly active mesoporous TiO2 nanoparticles, Journal of Environmental Sciences 43 (2016) 26-39. https://doi.org/https://doi.org/10.1016/j.jes.2015.05.033.

[113] I.K. Konstantinou, T.A. Albanis, Photocatalytic transformation of pesticides in aqueous titanium dioxide suspensions using artificial and solar light: intermediates and degradation pathways, Applied Catalysis B: Environmental 42(4) (2003) 319-335. https://doi.org/https://doi.org/10.1016/S0926-3373(02)00266-7.

[114] H.-S. Son, S.-J. Lee, I.-H. Cho, K.-D. Zoh, Kinetics and mechanism of TNT degradation in TiO2 photocatalysis, Chemosphere 57(4) (2004) 309-317. https://doi.org/https://doi.org/10.1016/j.chemosphere.2004.05.008.

[115] A. Elmelouky, A. Mortadi, E. Chahid, R. Elmoznine, Impedance spectroscopy as a tool to monitor the adsorption and removal of nitrate ions from aqueous solution using zinc aluminum chloride anionic clay, Heliyon 4(2) (2018) e00536. https://doi.org/https://doi.org/10.1016/j.heliyon.2018.e00536.

[116] J.V. Davis, O. Guio, B. Captain, C.D. Hoff, Production of cis-Na2N2O2 and NaNO3 by Ball Milling Na2O and N2O in Alkali Metal Halide Salts, ACS Omega 6(28) (2021) 18248-18252. https://doi.org/10.1021/acsomega.1c02119.

[117] S. Yeh, E.S. Rubin, M.R. Taylor, D.A. Hounshell, Technology Innovations and Experience Curves for Nitrogen Oxides Control Technologies, Journal of the Air & Waste Management Association 55(12) (2005) 1827-1838. https://doi.org/10.1080/10473289.2005.10464782.

[118] S. Wang, Q. Gao, X. Dong, Q. Wang, Y. Niu, Y. Chen, H. Jiang, Enhancing the Water Resistance of Mn-MOF-74 by Modification in Low Temperature NH3-SCR, Catalysts 9(12) (2019). https://doi.org/10.3390/catal9121004.

[119] S. Chen, Y. Zhou, J. Li, Z. Hu, F. Dong, Y. Hu, H. Wang, L. Wang, K.K. Ostrikov, Z. Wu, Single-Atom Ru-Implanted Metal–Organic Framework/MnO2 for the Highly Selective Oxidation of NOx by Plasma Activation, ACS Catalysis 10(17) (2020) 10185-10196. https://doi.org/10.1021/acscatal.0c02001.

[120] X. Wei, Y. Wang, Y. Huang, C. Fan, Composite ZIF-8 with CQDs for boosting visible-light-driven photocatalytic removal of NO, Journal of Alloys and Compounds 802 (2019) 467-476. https://doi.org/https://doi.org/10.1016/j.jallcom.2019.06.086.

[121] M. Chen, X. Wei, L. Zhao, Y. Huang, S.-c. Lee, W. Ho, K. Chen, Novel N/Carbon Quantum Dot Modified MIL-125(Ti) Composite for Enhanced Visible-Light Photocatalytic Removal of NO, Industrial & Engineering Chemistry Research 59(14) (2020) 6470-6478. https://doi.org/10.1021/acs.iecr.9b06816.

[122] J. Hu, Y. Ji, Z. Mo, N. Li, Q. Xu, Y. Li, H. Xu, D. Chen, J. Lu, Engineering black phosphorus to porous g-C3N4-metal–organic framework membrane: a platform for highly boosting photocatalytic performance, Journal of Materials Chemistry A 7(9) (2019) 4408-4414. https://doi.org/10.1039/C8TA12309H.

[123] M.Y. Mihaylov, V.R. Zdravkova, E.Z. Ivanova, H.A. Aleksandrov, P.S. Petkov, G.N. Vayssilov, K.I. Hadjiivanov, Infrared spectra of surface nitrates: Revision of the current opinions based on the case study of ceria, Journal of Catalysis 394 (2021) 245-258. https://doi.org/https://doi.org/10.1016/j.jcat.2020.06.015.

[124] M.T. Alam, N. Parvez, P.K. Sharma, FDA-Approved Natural Polymers for Fast Dissolving Tablets, Journal of pharmaceutics 2014 (2014) 952970. https://doi.org/10.1155/2014/952970.

[125] S. Selvakumaran, I. Muhamad, N.A. Md Lazim, Designing Polymeric Nanoparticles for Targeted Drug Delivery System, 2014, pp. 287-313.

[126] S.K. Papageorgiou, E.P. Kouvelos, E.P. Favvas, A.A. Sapalidis, G.E. Romanos, F.K. Katsaros, Metal–carboxylate interactions in metal–alginate complexes studied with FTIR spectroscopy, Carbohydrate Research 345(4) (2010) 469-473. https://doi.org/https://doi.org/10.1016/j.carres.2009.12.010.

[127] L. Pereira, A.M. Amado, A.T. Critchley, F. van de Velde, P.J.A. Ribeiro-Claro, Identification of selected seaweed polysaccharides (phycocolloids) by vibrational spectroscopy (FTIR-ATR and FT-Raman), Food Hydrocolloids 23(7) (2009) 1903-1909. https://doi.org/https://doi.org/10.1016/j.foodhyd.2008.11.014.

[128] J. Teixeira, V.F. Cardoso, G. Botelho, A.M. Morão, J. Nunes-Pereira, S. Lanceros-Mendez, Effect of Polymer Dissolution Temperature and Conditioning Time on the Morphological and Physicochemical Characteristics of Poly(Vinylidene Fluoride) Membranes Prepared by Non-Solvent Induced Phase Separation, Polymers, 2021.

[129] W. Zhao, X. Jin, Y. Cong, Y. Liu, J. Fu, Degradable natural polymer hydrogels for articular cartilage tissue engineering, Journal of Chemical Technology & Biotechnology 88(3) (2013) 327-339. https://doi.org/https://doi.org/10.1002/jctb.3970.

[130] J.P. Serra, A. Fidalgo-Marijuan, J. Teixeira, L. Hilliou, R. Gonçalves, K. Urtiaga, A. Gutiérrez-Pardo, F. Aguesse, S. Lanceros-Mendez, C.M. Costa, Sustainable Lithium-Ion Battery Separator Membranes Based on Carrageenan Biopolymer, Advanced Sustainable Systems 6(12) (2022) 2200279. https://doi.org/https://doi.org/10.1002/adsu.202200279.

[131] S. Zirak Hassan Kiadeh, A. Ghaee, M. Farokhi, J. Nourmohammadi, A. Bahi, F.K. Ko, Electrospun pectin/modified copper-based metal–organic framework (MOF) nanofibers as a drug delivery system, International Journal of Biological Macromolecules 173 (2021) 351-365. https://doi.org/https://doi.org/10.1016/j.ijbiomac.2021.01.058.

[132] R. Rezaee, M. Montazer, A. Mianehro, M. Mahmoudirad, Single-step Synthesis and Characterization of Zr-MOF onto Wool Fabric: Preparation of Antibacterial Wound Dressing with High Absorption Capacity, Fibers and Polymers 23(2) (2022) 404-412. https://doi.org/10.1007/s12221-021-0211-y.

[133] A. González, R. Contreras, G. Zuñiga, A. Moenne, Oligo-Carrageenan Kappa-Induced Reducing Redox Status and Activation of TRR/TRX System Increase the Level of Indole-3-acetic Acid, Gibberellin A(3) and trans-Zeatin in Eucalyptus globulus Trees, Molecules (Basel, Switzerland) 19 (2014) 12690-12698. https://doi.org/10.3390/molecules190812690.

[134] R. Majidi, J. Parhizkar, E. Karamian, Photocatalytic Removal of NOx Gas from Air by TiO2/Polymer Composite Nanofibers, Nanochemistry Research 3(2) (2018) 212-218. https://doi.org/10.22036/ncr.2018.02.011.

Declaration of interests

☒ The authors declare that they have no known competing financial interests or personal relationships that could have appeared to influence the work reported in this paper.

☐ The authors declare the following financial interests/personal relationships which may be considered as potential competing interests:

Highlights

+ Synthesised and characterised UiO-66, UiO-66-NH_2, MIL-125 and MIL-125-NH_2 MOFs

+ Demonstrated 100% NOx removal efficiency under UV light with NH2-functionalized MOFs

+ Proposed a NOX removal two stages mechanism based in adsorption and photooxidation

+ Achieved MOF immobilization in alginate/carrageenan for sustainable air filtration

+ Immobilisation into Membrane maintains MOF's ability to remove NOX from air

Journal Pre-proofs